The Development of Actuators for the Whole Skin Locomotion Robot

Eric Williams

Dissertation submitted to the Faculty of the

Virginia Polytechnic Institute and State University

in partial fulfillment of the requirements for the degree of

Doctor of Philosophy

in

Mechanical Engineering

Dennis W. Hong, Chair

Michael K. Philen

Brian Vick

Robert L. West

Christopher B. Williams

February 6th, 2014

Blacksburg, VA

keywords: helical springs, shape memory alloys, rod theory, contact, actuator

The Development of Actuators for the Whole Skin Locomotion Robot

Eric A. Williams

(ABSTRACT)

The Whole Skin Locomotion robot propels itself using a motion similar to the cytoplasmic streaming exhibited by an amoeba. In the robot there are embedded ring actuators which evert the material of the robot to produce forward motion. The robot benefits from a highly flexible exterior allowing it to squeeze into constricted passageways or collapsed structures. The development of actuators for such a motion is performed by a shape memory alloy composite actuator. Unlike a typical composite model which utilizes a homogenization of fiber and matrix properties our model is developed for line loads produced in individual shape memory alloy wires onto the rod structure. The load vectors are determined in the deformed configuration of the actuator to account for the highly deformed actuator profiles that would be seen in operation. Also the load requirements for such actuators are developed in terms of the constriction forces and functional design limits are established. In addition, a helical spring backbone design is considered and stiffness properties for general helical springs are determined. The contact of spring coils is included in the analysis and a coupled constitutive model is developed for the spring when coils are in contact. The static design of helical springs for use in the actuators is performed and deformation and load restrictions are determined for subsequent design efforts.

Acknowledgments

Of the many individuals who supported me through this endeavor I first want to thank my parents for their unconditional support and love. And without my fiance, Andrea, I can honestly say that I could not have achieved this milestone as her patience and love have kept me moderately sane through it all.

I also want to thank my advisor Dr. Hong for years of support and the flexibility to explore and learn for years under his guidance.

I want to thank my committee for both asking and answering many questions over my tenure here. Their thoughtful suggestions have helped me improve the quality and presentation of my work.

Also I certainly owe much thanks to my lab-mates who have been there through it all and have made a lab in a basement without windows seem like a home. This group of such smart and inspiring people has helped me grow in countless ways.

Contents

List of Figures

Chapter 1

Introduction

1.1 Motivation

The Whole Skin Locomotion (WSL) robot uses a motility mechanism inspired by the amoeba Fig. 1.1 [1]. The mechanism behind the amoeba's locomotion involves a cycling of material from the posterior to the anterior of the amoeba [1]. This motion could be considered as motion by a continuous extrusion of the interior.

The exterior of an amoeba is stationary during motion which allows the amoeba to move in the viscous environment of which it lives. The amoeba does not need to overcome viscous forces on its exterior in order to move relative to its environment. This motion is essentially similar to a wheel without slip; the point of contact of the wheel does not move relative to the ground yet cycles around the axle as the wheel moves forward.

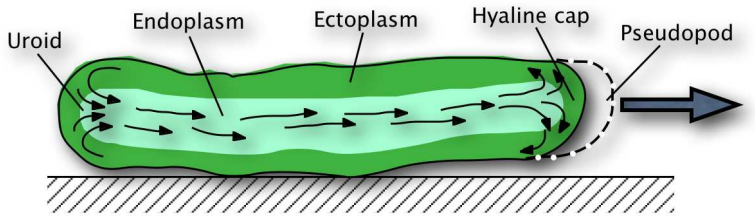

FIGURE 1.1: Amoeba using a pseudopod to move [1]

This same feature can be realized by an everting torus as in the WSL robot. The mechanism behind the WSL robot can be seen in Fig. 1.2. The continuous eversion of the WSL robot gives it a unique advantage in unstructured terrain and nearly collapsed environments.

The benefits of an external "tank tread" for mobile robots have been demonstrated by many researchers in the field. The WSL robot utilizes a traction surface over its entire exterior will allow it to traverse increasingly more complicated terrain in comparison to previous attempts to develop a tread-like surface [2]. The Omnitread robot developed at the University of Michigan employs discrete treads over the exterior surface of a segmented snake robot [3].

Medical Robotics

Minimally invasive surgery has provided a new area of application to roboticists [4]. The complicated domain inside the human body requires robust and bio-compatible robotic manipulators to be used in surgery. The manipulation of tissues and objects inside the body requires feedback mechanisms such as force or displacement to limit forces on the sensitive

tissues inside the body or to provide accurate forces for cutting or grasping [5].

Visual feedback is usually sought out such that exploratory measures can be performed along with a biopsy to determine a prognosis. Endoscopes are a commonly used device which can be fed into the body through an orifice such that images may be taken of the internal tissues of the body. It is now possible that video recording devices can be swallowed which can collect image data of the inside of the gastrointestinal tract or injected into other cavities in the body [6] [7].

However, swallowing a passive imaging device has disadvantages. A passive device would pass through the body and take images only along its trajectory through the body without ability to focus on details within the body which are of major concern. This means that the images collected may not contain enough information about the area of interest. Active robotic solutions enable a more directed look at areas of interest. This has spurned a whole field of mobile robots which offer the mobility requirements within the body and add the potential for drug delivery at precisely the point of need [6][8].

In addition to the collection of images local to a probe or scope it is possible to collect high fidelity images from outside the body using magnetic resonance imaging and computed tomography scans to map the interior of the body. Surgeries have now been conducted that utilize the feedback of external imaging devices along with the surgery to aid in the visualization during surgical procedures [9].

The treatment of short bowel syndrome has recently found an application for SMAs [10].

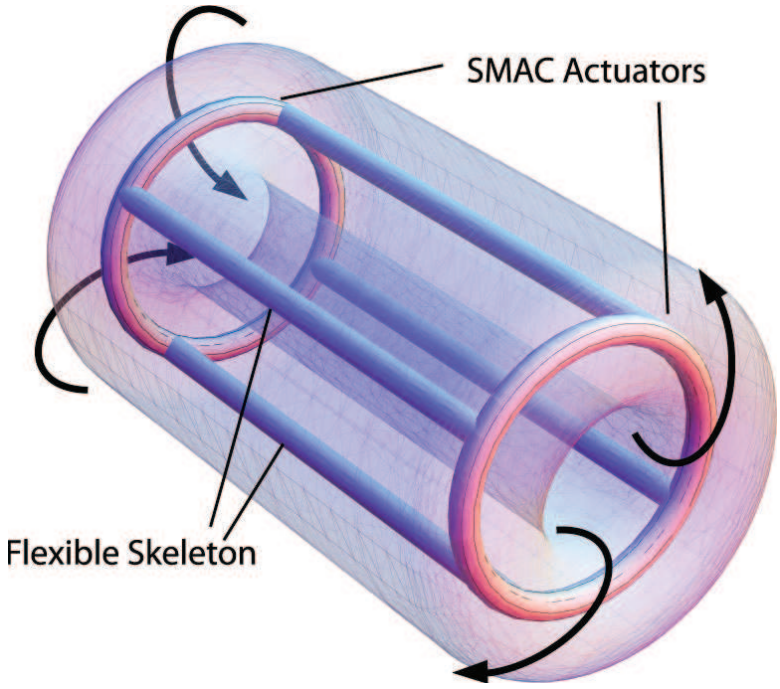

FIGURE 1.2: WSL robot showing the embedded actuators and the eversion mechanism

In their work Utter et al. developed a device to put stress on the bowel in situ and this stress has been found to increase the growth rate of the bowel significantly [10].

1.1.1 WSL Actuator

The outer shell of the robot is a continuous elongated torus as shown in Fig. 1.2. The robot is essentially a continuous 3D tank tread which is everted by forces generated inside the robot.

The actuators are in the shape of a ring torus and transmit loads from the ring actuators to the outer shell Fig. 1.3.

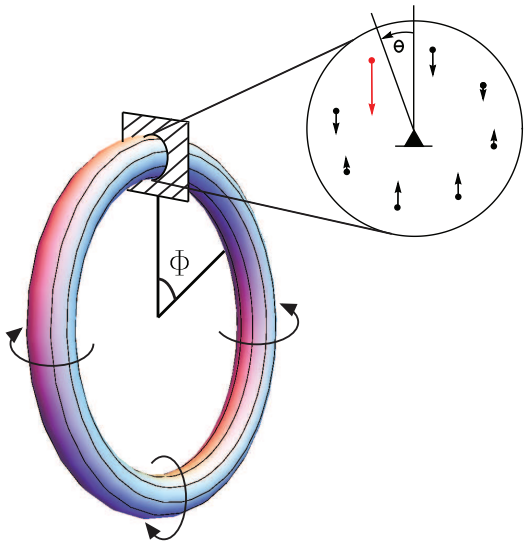

FIGURE 1.3: Torus actuator showing the contracting SMA wire in red

Eversion of WSL robot

The development of the Whole Skin Locomotion (WSL) robot requires the development of actuation mechanisms by which the eversion motion can occur. Eversion is the continuous motion of turning inside out, such as the inversion of a tube (Fig. 1.4). The everting process can be used as a means to move the WSL robot through unstructured terrain. Since the WSL robot is designed to be capable of traversing unstructured environments, exterior flexibility will enable the passage through tight spaces and around obstacles.

In order to produce this complex motion it is necessary to develop actuators which can generate the required forces within the elongated torus exterior. Previously, several designs were considered to make such a motion [1][2]. Flexible actuators are required which can operate while in a highly deformed state as actuation forces are increasingly important in a

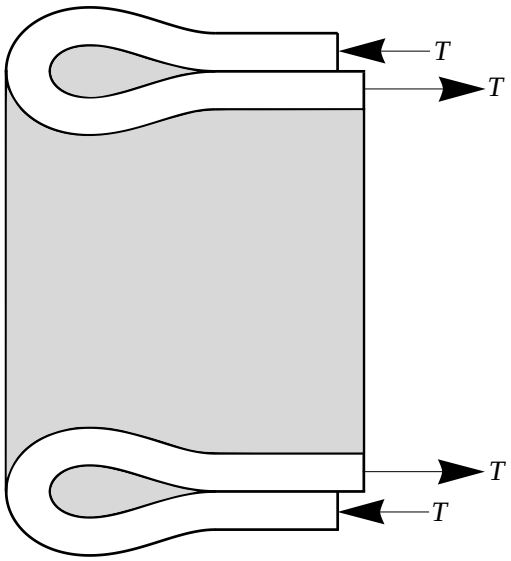

FIGURE 1.4: A section view of partial eversion of a tube

collapsed state.

In that work it was shown that a SMA fiber composite torus could produce actuation forces. The properties of actuation were described and basic models of the process were presented. In that work, an assumption of axisymmetric loading was made that allowed simplified representations of the actuating torque.

A limitation of that analysis is that the axisymmetric assumption limits the analysis to problems of symmetric loading and does not provide sufficient allowances for large in plane or out of plane loads or deformations. In order to traverse collapsed environments, the robot and the actuators must deform via several combined modes. Since one of the main benefits of the WSL robot is that it can deform to its environment and traverse collapsed or narrow passageways, it is required that it should deform asymmetrically with the potential for out

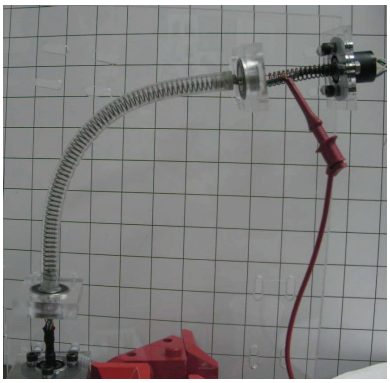

FIGURE 1.5: Prototype constructed for qualitative experiments

of plane motions.

This work involved constructed prototypes comprised of PDMS-SMA composite rods. Qualitative experiments demonstrated the ability for a torus segment to evert as current was applied to one of the SMA wires (Fig. 1.5).

For the following studies the methods of continuum mechanics will be utilized to describe the behavior of the actuator. The description of motion of a spatially curved rod is quite complex outside of the simple axisymmetric and planar cases. The governing equations for a loose wire composite rod using a continuum approach will be presented in Chapter 3.

1.2 Related Works

The WSL robot is a mobile robot that is developed to access spaces where traditional wheeled or legged robots cannot go reliably. The robot may serve multiple purposes upon reaching its destination within some confined space. Applications for the WSL robot are found in

medical robotics, search and rescue robotics, reconnaissance and mineral extraction.

The principle of the WSL robot has cousins within the robotics community. The toroidal snake robot by McKenna et al. utilizes a fabric exterior and worm gear drive to provide locomotion in unstructured terrain [11]. And for the past 20 years there has been a strong push within medical robotics in order to develop tele-operated surgical robots [12].

1.2.1 Robot Manipulators

Flexible robotic manipulators have been under investigation for the past two decades. They offer advantages over rigid body robots in tasks when soft contact must be made with objects in their environment. Also they have increasingly complex workspaces in which they can operate allowing them access in tasks such as minimally invasive surgery [13][12][5].

The ability for conformal grasping and tele-operated surgical tools have brought about many advances in continuum robots over the past twenty years. Ota et al. developed the Cardio-arm surgical manipulator for assisting in thoracic surgery [14]. Rucker et al. developed active cannular robot manipulators which use nested elastic tubes for producing highly articulate motions for minimally invasive surgery [15]. Xu and Simaan have investigated intrinsic force sensing through structural deformation sensing [16].

Past researchers have used soft materials, springs or a series of universal joints to achieve their desired motion profiles [17]. Compliant mechanisms such as live hinges and soft material linkages have enabled the production of various robotic manipulators [18][19].

Several researchers have utilized transmission mechanisms to deliver loads to the robotic manipulator from outside of the robot via cables, pneumatic pressure or [20][21][15][22][18]. This makes such systems inherently less modular. For cable driven or cannular methods, the loads that must be produced must increase since an increase in transmission distances leads to an increase in frictional loads. Another side effect of such systems is their inherent stiffness and the stiffness of the transmission systems. The increase in transmission distance requires stiffer transmission systems which reduces the likelihood for the overall manipulator to remain flexible.

The ability for robots to be flexible has trade-offs as the design process is further complicated for both the structural design and controller design [23]. Also the degree of flexibility introduces the potential for stability issues. The stiffness parameters become more complicated as loading histories become more complex. These difficulties can be lessened with the proper use of continuum mechanics as a backbone for the model development.

1.2.2 SMA Actuators

The requirement for mobile robots to be lightweight and modular has lead many researchers to explore shape memory alloys or other smart materials. The relative energy density of shape memory alloys is hard to neglect when seeking an actuation mechanism [24].

Shape memory alloys (SMAs) have long been considered promising candidates for actuating structures such as plates, shells and rods [25][26]. SMAs exhibit the shape memory

effect whereby strain can be recovered and constrained recovery forces are generated that allow the material to do work. They have the ability to generate large forces and large strains making them excellent candidates for structural actuation.

SMAs offer high power density so they are great for miniaturization of existing actuators. SMAs can provide various types of loads depending on their configuration and can act as ultra-compact linear actuators when utilized simply in wire form. Many applications have been found to utilize SMA as actuated tendons [27].

1.3 Objectives

The main objective of this work is to develop an actuation strategy for the WSL robot. In order to achieve this main goal we have outlined various intermediate steps towards this end. Firstly, the kinematic description of the eversion motion is required to understand the structure of the motion and what types of supports enable the required abilities. Secondly, the load requirements for the actuation mechanisms must be developed such that a designer can select actuator properties to match a particular embodiment of our design. Thirdly, the structure must be designed to meet the aforementioned criteria. Lastly such a design should be simulated and experiments should be designed to determine the total system performance.

For the work at hand the first three objectives have been met and the fourth was partially completed with the experiments as the last outstanding task. The author intends to achieve such experiments as subsequent funding becomes available.

1.4 Contributions

The major contributions of this research endeavor are the following

- Development of everting ring actuators utilizing line loads
- Formulation of loose wire composite actuator model
- Homogenization of a helical spring model as a extensible rod
- Development of a design methodology for the helical spring backbone for the composite

1.5 Dissertation Overview

This chapter presented the motivation for the Whole Skin Locomotion (WSL) robot. The robot's eversion mechanism has been developed within the context of current mobile robots and continuum robots.

Chapter 2 considers the bending of cylindrical rods. The theory developed herein demonstrates the ability to describe the eversion motion as a set of possible equilibrium positions of a symmetric beam. The eversion torque is explored through the eversion of a ring with curvature in the reference configuration.

Chapter 3 discusses the modeling of Shape Memory Alloy Composite (SMAC) rods. The composite is considered both as a fully bonded composite and also as a case where the

fibers are able to move relative to the matrix. The introduction of nonlinear string theory is presented such that line loads can be described between the matrix and the fibers.

Chapter 4 discusses modeling and simulation efforts used to develop a framework to design helical springs for use as a backbone for the shape memory alloy composite actuators.

Chapter 5 develops design equations for helical springs as a backbone for the actuation mechanism. Static failure theories are applied to the combined bending and torsion of helical springs for use in the composite actuators.

To conclude the dissertation, Chapter 6 discusses several short studies and future works.

Chapter 2

Deformations of Cylindrical Rods

2.1 Background

The WSL robot is a mobile robot that benefits from having a continuous treading surface on its exterior. The robot is also highly deformable to allow it passage through crevices and holes smaller than its nominal height and diameter. And similar to a tire, the robot uses friction to deliver torque to the ground and provide thrust force.

The development of the actuators for the WSL robot requires a model to describe the behavior of the external structure and the required forces that must be generated to produce thrust forces. In the case of the WSL robot, thrust forces must be generated regardless of the deformed state of the robot to allow passage through narrow openings or around and between obstacles. In Fig. 2.1 two such toroidal actuators are shown, although it is possible

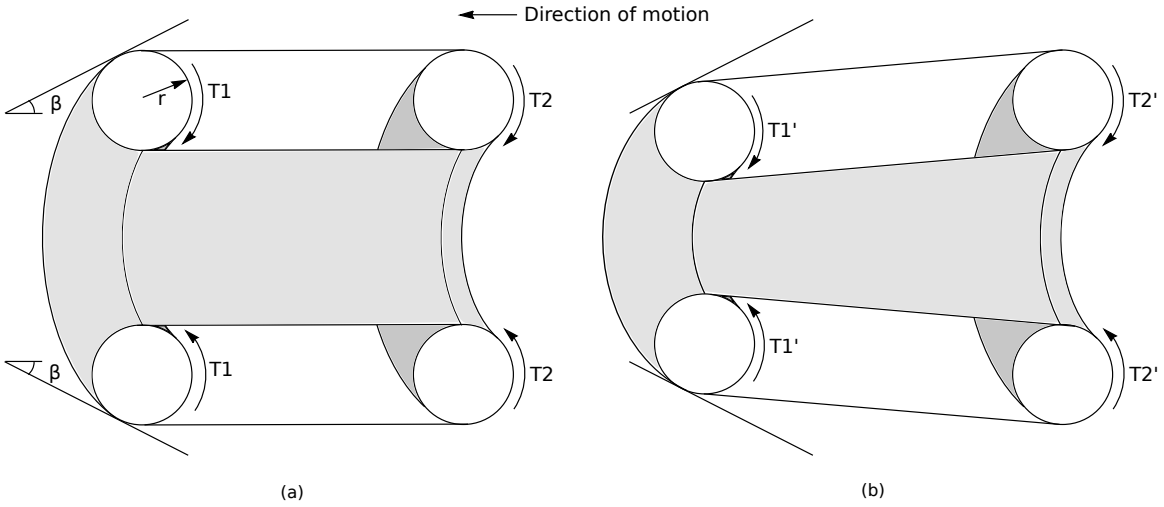

FIGURE 2.1: Section view of the WSL robot, a.) before deformation b.) in a deformed state

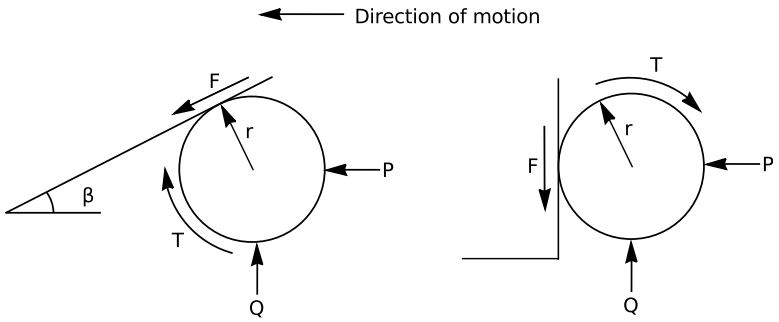

FIGURE 2.2: Free body diagram of the WSL robot and obstacles

to include several actuators.

The required forces that the robot must utilize to make passage through collapsed or restricted spaces increase as the robot deforms to its environment. The frictional force between the robot and obstacles can be seen in Fig. 2.2. Frictional force must be sufficient to provide torque transfer and thrust forces to be generated in the robot. If the friction is not high enough then the robot will not be able to pass through a given obstacle.

The general free body diagram for the robot actuator is depicted in Fig. 2.2a. The

operation of the robot on flat terrain without obstacles is the simplest case and is included as a special case when the angle β goes to zero. When the robot encounters a blunt obstacle ($\beta = \pi/2$) as depicted in Fig. 2.2b, the additional force, P, becomes necessary since a torsional applied load is not sufficient to pass a blunt obstacle with zero normal force. The frictional force is assumed to be a function of the normal force

$$\vec{F} = \mu \vec{N} \tag{2.1}$$

where μ is the coefficient of friction. The coefficient of friction, μ, is valid for static and dynamic loads, but its magnitude typically changes at the onset of slip. For a comparison of various friction models see Dupont et al. [28].

Using the free body diagram in Fig. 2.2 one can solve for the torque and the coefficient of friction that is required such that slipping does not occur.

$$T = \mathrm{Q\ r}\ \sin(\beta) - \mathrm{P\ r}\ \cos(\beta) \tag{2.2}$$

$$\mu \geq 2\left(\frac{\mathrm{Q}\ \tan(\beta) - \mathrm{P}}{\mathrm{Q} + \mathrm{P}\ \tan(\beta)}\right) \tag{2.3}$$

The static problem is completely described if the torque T and the forces P and Q are known a priori. The torque, T, is the everting torque generated by the actuators and will be one of the design variables of the WSL actuators. The force Q is the force due to in-plane loads such as bending and constriction of the actuators. The force Q will be another design variable in the problem and its further relevance will be explained in the next section. The force P is the net thrust force of the posterior end of the robot and can be generated by one or more actuators acting in series.

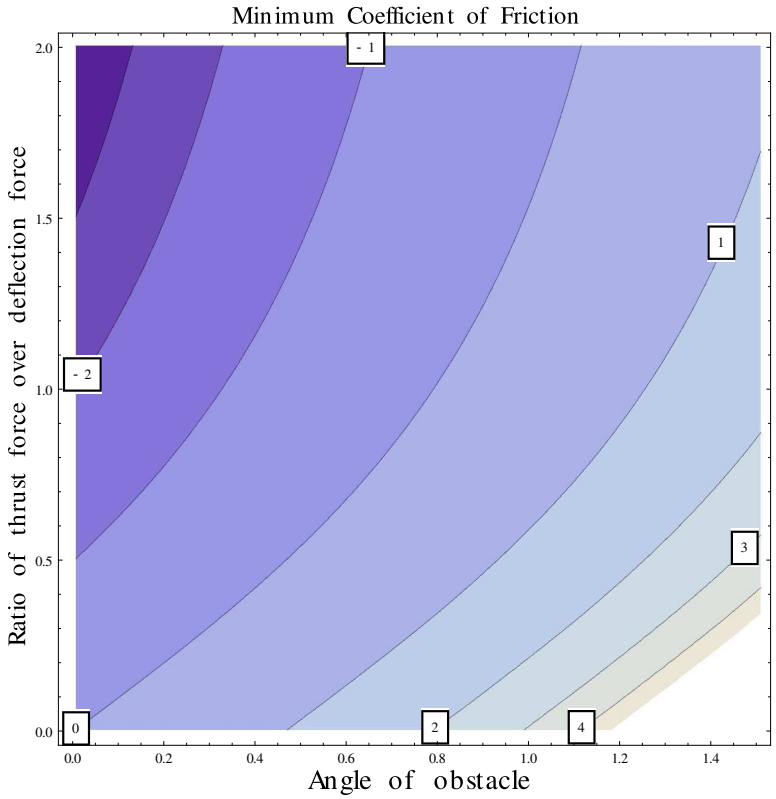

FIGURE 2.3: Contour plot of the minimum coefficient of friction

For a blunt contact such as when β goes to $\pi/2$ (Fig. 2.2b) the minimum coefficient of friction requirement increases and is show in Eq. 2.4. This equation also demonstrates that the thrust force, P, must be high in order to enable passage of obstacles with realistic values for the coefficient of friction.

$$\mu >= \frac{2Q}{P} \tag{2.4}$$

The coefficient of friction between the exterior of the robot and the environment is kept as high as possible by utilizing rubber for the robot exterior. The possibility of having tread or raised surfaces is also a possibility, but this will not be considered a major aspect of the design.

The force Q mentioned in the last section is generated as the structure deforms to achieve obstacles. The magnitude of the deflection force, Q, can be determined by the stress in the structure due to the deflection. Also, the actuators are designed to be flexible in order to squeeze through narrow passageways. This implies that the deflection force, Q, must be kept small.

The stress state in an elastic structure undergoing finite deformations requires the solution of the governing equations in the deformed configuration. This typically requires the solution of nonlinear partial differential equations by numerical methods such as Finite Element Analysis or Finite Difference methods. These methods can be time intensive and computationally expensive. In order to reduce computation time and develop design guidelines it is beneficial to solve reduced dimensional models such as shell or rod theories. The nonlinearities associated with finite deformations will typically still require numerical methods, but the aim should be to use semi-analytical methods whenever possible if exact solutions are not possible [29] [30].

The geometry of the actuators are depicted in Fig. 1.3. The aspect ratio of the torus actuators allow their representation as slender rods. The description of the actuators as rods reduces the complexity of the solution methods while retaining their bulk behavior. Note that large deformation beams are synonymous with rods. The terms have been interchanged throughout literature and a thorough search must include both terms [29][31][32]

2.2 Rods

A rod or beam is a deformable structure, that is of the simplest order allowing 3D spatial deformations [29]. The properties of the deformed structure can be described solely in terms of a parameter (typically taken to be the arc length). This enables the reduction of the governing equations from partial differential equations to nonlinear ODEs which can be solved readily using numerical methods.

The modern reference for the theories of rods is from Antman [29]. Antman's treatise on nonlinear elasticity dedicates much of the book to the development of nonlinear rod theories and makes references to both old and new works [29].

Many rod theories exist, which have constraints on their deformation. One such constraint is the in-extensibility of the axial curve. This requires that the rod cannot be strained along its axial curve regardless of the loads applied. Another constraint is that of a shear inflexibility which guarantees plane sections remain plane. For more details on constrained rod theories, see Antman [29].

Kirchhoff rods are a constrained rod theory that the rods where shear deformations are neglected. Due to the simplifying assumptions it is usually taken as a first approximation to the solution of problems regarding rod-like bodies [31]. Applications of the static theory of inextensible Kirchhoff Rods are presented in detail by Svetlitsky [33]. Svetlitsky also demonstrates applications of the dynamic theory of Kirchhoff rods in another book [34]. Tadjbakhsh and Lagoudas developed a variational theory of extensible Kirchhoff rods which

is another form of a constrained rod theory[35].

The further use of "rods" will henceforth refer to Kirchhoff rods unless specifically stated. The rods will also be considered inextensible unless otherwise noted.

The governing equations for rods include the equations of motion, the kinematic relations, the constitutive relations and the boundary conditions. These equations constitute a full set such that the solutions can be found for the initial boundary value problems of the deformation of rods.

2.2.1 Kinematics

The configuration of a rod in three dimensions is described by the position of the axial curve in 3D space. Rods may be characterized using curvilinear coordinates in both the reference configuration and the deformed configuration. The use of curvilinear coordinates in rod theory is readily performed using elements from differential geometry [36] [37] [38] . In order to determine deformation parameters it is necessary to select appropriate coordinate frames for the reference and deformed configurations respectively. For a thorough treatment of curvilinear coordinates in finite elasticity see Green and Zerna [32].

The deformed configuration is represented by a set of base vectors that change as the body deforms. The description of motion for inextensible rods can be described solely by the rotations of the axial curve as the base vectors change from the reference location to the deformed configuration. The deformed base vectors, $\vec{e}$, can be described by an orthogonal

matrix, L, and the original base vectors $\vec{e}_0$ (Eq. 2.5).

The orthogonal transformation matrix, L, can be selected by prescribing a set of Euler angles [33]. The selection is not distinct and care should be taken to avoid singularities wherever possible. For the following development a 1-3-2 rotation sequence is selected (Eq. 2.6). This essentially means that a rotation is first done about the x-axis, then the z axis and followed y by a rotation in the y-axis (Eq. 2.6).

$$\vec{e} = [\mathrm{L}]\,\vec{e}_0 \tag{2.5}$$

$$[\mathrm{L}] = \begin{pmatrix} \cos(\theta_2) & 0 & -\sin(\theta_2) \\ 0 & 1 & 0 \\ \sin(\theta_2) & 0 & \cos(\theta_2) \end{pmatrix} \begin{pmatrix} \cos(\theta_3) & \sin(\theta_3) & 0 \\ -\sin(\theta_3) & \cos(\theta_3) & 0 \\ 0 & 0 & 1 \end{pmatrix} \begin{pmatrix} 1 & 0 & 0 \\ 0 & \cos(\theta_1) & \sin(\theta_1) \\ 0 & -\sin(\theta_1) & \cos(\theta_1) \end{pmatrix} \tag{2.6}$$

The result from Eq. 2.6 can be expressed in a more explicit form (Eq. 2.7).

$$[\mathrm{L}] = \begin{pmatrix} \cos(\theta_2)\cos(\theta_3) & \sin(\theta_1)\sin(\theta_2) + \cos(\theta_1)\cos(\theta_2)\sin(\theta_3) & -\cos(\theta_1)\sin(\theta_2) + \cos(\theta_2)\sin(\theta_1)\sin(\theta_3) \\ -\sin(\theta_3) & \cos(\theta_1)\cos(\theta_3) & \cos(\theta_3)\sin(\theta_1) \\ \cos(\theta_3)\sin(\theta_2) & -\cos(\theta_2)\sin(\theta_1) + \cos(\theta_1)\sin(\theta_2)\sin(\theta_3) & \cos(\theta_1)\cos(\theta_2) + \sin(\theta_1)\sin(\theta_2)\sin(\theta_3) \end{pmatrix} \tag{2.7}$$

Vectors in the reference configuration and the deformed configuration can be described by either set of base vectors Eq. (2.8). The components a_i in the deformed basis and the components a_{0j} in the reference basis are generally not equal, however the magnitude of the vector is invariant in any coordinate basis.

$$\vec{a} = a_i\vec{e}_i = a_{0j}\vec{e}_{0j} \tag{2.8}$$

The base vectors used to represent rods are an orthogonal triad of vectors. The Frenet frame of reference is a potential candidate to describe rod motion due to its simplicity[38]. The Frenet frame uses the tangent, the normal and the binormal to the axial curve as its base vectors[38]. The change in the direction of the Frenet frame with respect to the arc length can be shown to be

$$\frac{d}{ds}\begin{Bmatrix} \vec{t} \\ \vec{n} \\ \vec{b} \end{Bmatrix} = \begin{pmatrix} 0 & \kappa & 0 \\ -\kappa & 0 & \tau \\ 0 & -\tau & 0 \end{pmatrix} \begin{Bmatrix} \vec{t} \\ \vec{n} \\ \vec{b} \end{Bmatrix} \tag{2.9}$$

where $\vec{t}$,$\vec{n}$,$\vec{b}$ are the tangent, normal and binormal vectors respectively. The additional quantities κ and τ are the curvature and the torsion of the curve. It will be shown later that the curvature and torsion of the curve are invariants which can be used to describe the strain at a point in the body [38].

The Frenet frame is convenient whenever the problem geometry has a circular cross section or the principal axes of the cross section coincides with the normal and the binormal to the curve. However, another rotated frame must be developed since this is not true in general. The rotated frame is called the Darboux frame and can be constructed by an additional rotation, θ_1, of the Frenet frame about its tangent direction $\vec{t}$ (Eq. 2.10, Fig. 2.4) [33]. The benefits of the frame is that it can track torsional deformation and provide the possibility for a pre-twisted rod with principal axes of symmetry in the cross section (ie. a

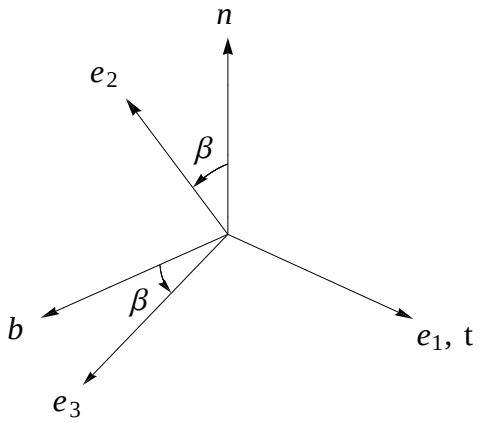

FIGURE 2.4: Rotation of the Frenet frame produces the Darboux frame

drill bit).

$$\begin{Bmatrix} \vec{e}_1 \\ \vec{e}_2 \\ \vec{e}_3 \end{Bmatrix} = \begin{pmatrix} 1 & 0 & 0 \\ 0 & \cos[\theta_1] & \sin[\theta_1] \\ 0 & -\sin[\theta_1] & \cos[\theta_1] \end{pmatrix} \begin{Bmatrix} \vec{t} \\ \vec{n} \\ \vec{b} \end{Bmatrix} \tag{2.10}$$

The change in the direction of the Darboux frame with respect to the arc length can be shown to be

$$\frac{d}{ds}\begin{Bmatrix} \vec{e}_1 \\ \vec{e}_2 \\ \vec{e}_3 \end{Bmatrix} = \begin{pmatrix} 0 & -æ_3 & æ_2 \\ æ_3 & 0 & -æ_1 \\ -æ_2 & æ_1 & 0 \end{pmatrix} \begin{Bmatrix} \vec{e}_1 \\ \vec{e}_2 \\ \vec{e}_3 \end{Bmatrix} \tag{2.11}$$

where $æ_i$ are the Darboux curvatures. The Darboux curvatures, $æ_i$, are related to the

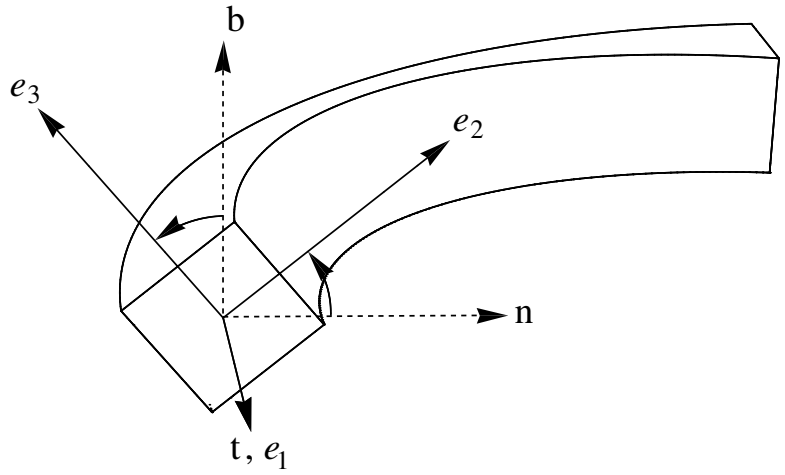

FIGURE 2.5: A bent and twisted rod showing the the Frenet frame and the Darboux frame

curvature and torsion of the curve by

$$\begin{aligned} æ_1 &= \tau + \frac{d\theta_1}{ds} \\ æ_2 &= \kappa \sin[\theta_1] \\ æ_3 &= \kappa \cos[\theta_1] \end{aligned} \tag{2.12}$$

where θ_1 is the combination of natural twist in the rod and the twist due to deformation. Note that the Darboux frame makes it possible to specify the coordinate frame with respect to a detail such as an axis of symmetry in the cross section that may twist along the main generator.

In this study, the Darboux frame is used to track the positions of the wire in the deformed configuration. The position of the wires is critical in determining the torque generated by the distributed load that the wires apply to the rod.

Displacements of Rod Axis

Describing the displacement of the rod axis is a simple problem once the equations representing the change in bases are established. The rod axis is represented by a material vector, $\vec{e}_0$, and $\vec{e}$ in the undeformed and the deformed configuration respectively. The displacement of a point on the rod axis is described as

$$\vec{u} = \vec{r} - \vec{r}_0 \tag{2.13}$$

where $\vec{r}$ and $\vec{r}_0$ are the position vectors for the point in the deformed and undeformed configurations respectively. The derivative of the displacement vector $\vec{u}$ with respect to arc length is equivalent to the change in the tangent between the undeformed and deformed configurations (Eq. 2.14).

$$\frac{d\vec{u}}{ds} = \frac{d\vec{r}}{ds} - \frac{d\vec{r}_0}{ds} = \vec{e}_1 - \vec{e}_{01} \tag{2.14}$$

The transformation in Eq. 2.5 is then applied to reduce Eq. 2.14 to the form

$$\frac{d\vec{u}}{ds} = (1 - l_{11})\vec{e}_1 - l_{21}\vec{e}_2 - l_{31}\vec{e}_3 \tag{2.15}$$

where l_{ij} are the components of the rotation matrix L from Eq. 2.5.

Strain Measures in Rod Theory

The strain measures used in inextensible rod theory are the local change in angles of the axial curve of the rod. This means that the Euler angle representation used in Eq. 2.5 is

linked to the change in curvatures from the reference to the deformed configurations. This requires that a relationship must be established between the changes in the Euler angles and the curvatures in the reference and deformed configurations.

Using Eq. 2.5 with a pre-multiplication by the transpose of the rotation matrix, L, the reference bases can be put in terms of the deformed bases.

$$\vec{e}_0 = [L]^T \vec{e} \tag{2.16}$$

The deformed bases are differentiated with respect to arc length. The rotation matrix, L, is a function of arc length, so the product rule of calculus is applied yielding Eq. 2.17.

$$\frac{d\vec{e}}{ds} = \frac{d[L]}{ds}\vec{e}_0 + [L]\frac{d\vec{e}_0}{ds} \tag{2.17}$$

Upon substituting the result from Eq. 2.11 to the terms of $\frac{d\vec{e}}{ds}$ and $\frac{d\vec{e}_0}{ds}$ Eq. 2.17 takes the form

$$\begin{pmatrix} 0 & -æ_3 & æ_2 \\ æ_3 & 0 & -æ_1 \\ -æ_2 & æ_1 & 0 \end{pmatrix} \vec{e} = \frac{d[L]}{ds}\vec{e}_0 + [L] \begin{pmatrix} 0 & -æ_{03} & æ_{02} \\ æ_{03} & 0 & -æ_{01} \\ -æ_{02} & æ_{01} & 0 \end{pmatrix} \vec{e}_0 \tag{2.18}$$

where the terms $æ_{0i}$ are the initial curvatures of the rod in the reference configuration. If $\vec{e}_0$ and $\vec{e}$ are eliminated using Eq. 2.16 and the remaining bases are factored out then Eq. 2.18 takes the form

$$\begin{pmatrix} 0 & -æ_3 & æ_2 \\ æ_3 & 0 & -æ_1 \\ -æ_2 & æ_1 & 0 \end{pmatrix} = \frac{d[L]}{ds}[L]^T + [L] \begin{pmatrix} 0 & -æ_{03} & æ_{02} \\ æ_{03} & 0 & -æ_{01} \\ -æ_{02} & æ_{01} & 0 \end{pmatrix} [L]^T. \tag{2.19}$$

The terms in Eq. 2.19 involving the derivatives of L can be evaluated using the chain rule of calculus. The skew symmetric nature of Eq. 2.19 can be utilized to reduce the description to only three distinct equations for $æ_i$. For a detailed derivation see the appendix in Svetlitsky [33]. The end result of this process gives the relation

$$æ_i = [L_1]_{ij}\frac{d\theta_j}{ds} + [L]_{ij}æ_{0j} \tag{2.20}$$

$$[L_1] = \begin{pmatrix} \cos[\theta_2]\cos[\theta_3] & 0 & -\sin[\theta_2] \\ -\sin[\theta_3] & 1 & 0 \\ \sin[\theta_2]\cos[\theta_3] & 0 & \cos[\theta_2] \end{pmatrix} \tag{2.21}$$

where the matrix L_1 has been introduced and the local derivatives of the Euler angles, $\frac{d\theta_j}{ds}$, have surfaced. This completes the kinematic analysis of the theory of rods. The relationship in Eq. 2.20 provides a set of first order ODEs relating the change in curvature to the change in Euler angles.

2.2.2 Equilibrium of Rods

The description of equilibrium in rod theory utilizes stress resultants instead of actual stresses. This allows the use of equipotent load systems consistent with the St. Venant principle [31]. Rod theory describes the stress and deformation in terms of a single independent variable. The independent variable for rod calculations is the undeformed arc length parameter, but this does not limit the rod to be inextensible.

Since a rod can be curved and twisted in its reference configuration, the derivatives of vector forces and moments with respect to arc-length must be included. To be as general as possible, the equilibrium equations are described in the deformed Darboux frame presented in the previous section.

Equilibrium is enforced in the present configuration, so the curvatures ($æ_i$) are considered unknown functions of the arc-length parameter and must be determined using a constitutive model. The curvature components may be assembled into a vector form

$$\vec{æ} = æ_i \vec{e}_i \tag{2.22}$$

where $æ_i$ are the deformed curvature components and $\vec{e}_i$ are the base vectors in the deformed reference frame. The equilibrium equations shown in Eq. 2.23 are cast in the deformed reference frame [33].

$$\begin{aligned} \frac{d\vec{Q}}{ds} + \vec{P} = \frac{\breve{d}\vec{Q}}{ds} + \vec{æ} \text{ x } \vec{Q} + \vec{P} = 0 \\ \frac{d\vec{M}}{ds} + \vec{e}_1 \text{ x } \vec{Q} + \vec{T} = \frac{\breve{d}\vec{M}}{ds} + \vec{æ} \text{ x } \vec{M} + \vec{e}_1 \text{ x } \vec{Q} + \vec{T} = 0 \end{aligned} \tag{2.23}$$

In Eq. 2.23, the symbol, $\frac{\breve{d}()}{ds}$, has been introduced to represent the local derivative. This is treated as the change in the component of a vector quantity as the direction is held constant. The concept of the local derivative occurs in curvilinear coordinates where the change in base vectors must be considered. This derivative only acts on the components whereas the term involving curvature is the derivative of the base vector (Eq. 2.11). Another sense of this derivative is the covariant derivative from tensor calculus which arises in any curvilinear coordinate system [36].

Constitutive relations for Isotropic Rods

Constitutive models predict the stress in a body due to strain. A linearly elastic isotropic material can be shown to have the following constitutive law

$$\sigma_{ij} = 2\mu\varepsilon_{ij} + \lambda\varepsilon_{kk}\delta_{ij} \tag{2.24}$$

where μ and λ are the Lame constants for the material. They can cast into terms of the Young's Modulus and Poisson's ratio by the following relation

$$\begin{aligned} \lambda &= \frac{E\nu}{(1+2\nu)(1-2\nu)} \\ \mu &= \frac{E}{2(1+\nu)} \end{aligned} \tag{2.25}$$

where E and ν are the Young's modulus and Poisson's ratio respectively.

The Euler-Bernoulli beam approximation is often made to simplify the constitutive relationship such that stress in a bending beam is generated along the axis of the beam and that stress is

$$\sigma_{11} = E\epsilon_{11} = E(\epsilon_0 - y\kappa_z + z\kappa_y). \tag{2.26}$$

Stress Resultants

As in beam or shell theory, the determination of stress resultants are required in rod theory [39]. The stress in an elastic body is put into terms of the strain and integration over the area of the cross section are performed in order to get the values for the particular resultants. The stresses on the cross section of the rod are integrated to generate resultant forces and

moments.

$$Q_1 = \int_S \sigma_{11} da = E \int_S (\epsilon_0 - x_2\kappa_3 - x_3\kappa_2) da \tag{2.27}$$

$$M_1 = \int_S (x_2\sigma_{13} - x_3\sigma_{12}) da \tag{2.28}$$

$$M_2 = \int_S x_3\sigma_{11} da = E \int_S x_3(\epsilon_0 - x_2\kappa_3 - x_3\kappa_2) da \tag{2.29}$$

$$M_3 = \int_S x_2\sigma_{11} da = E \int_S x_2(\epsilon_0 - x_2\kappa_3 - x_3\kappa_2) da \tag{2.30}$$

The geometric properties that involve the physical dimensions of the structure are inputs to the second moments of area for the cross section, (I_2, I_3), and the geometric torsional constant, J_1. For circular sections, J_1 reduces to the polar moment of area. The matrix A is the diagonal matrix containing J_1,I_2 and I_3.

$$\vec{M} = [A]\,(\vec{\text{æ}} - \vec{\text{æ}}_0) \tag{2.31}$$

For an inextensible rod theory the generation of strain energy is due only to bending moment as shown in Eq. 2.31. The shear stress resultants, $\vec{Q}$ are determined from the solution of the equilibrium equations.

This completes the formulation for the governing equations for rods. The system of ODEs are presented in Appendix B (Eq. 6.18). The solution of several problems for isotropic rods are provided in the next section.

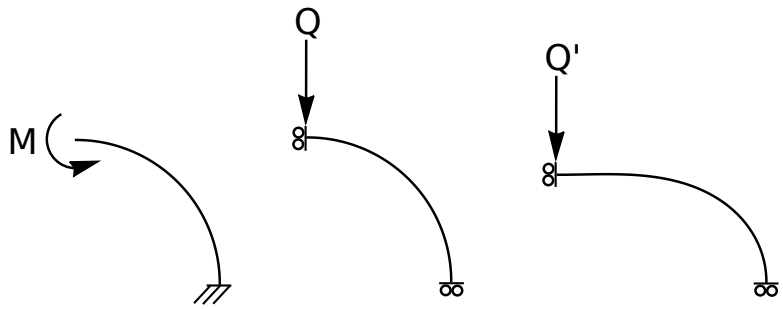

FIGURE 2.6: Three configurations of the rod at various loading steps

2.3 Simulations

In order to simulate a collapsed environment several potential deformation modes are selected and analyzed. The first type of subsequent loading is the deflection by an end load as in Fig. 2.6. This mode demonstrates the state of stress in the rod when impinged by an opening which narrows as the robot squeezes its way forward. As was described earlier in this chapter, the external forces are due to the robot's motion through an obstacle or as it climbs up an inclined plane.

Model symmetry is utilized when possible to reduce the computation time and in the case of this simulation a quarter model of the torus is studied. Also the assumption of planar behavior allows a simplified model to be computed using the equilibrium equations for planar rods which reduce the number of dependent variables from 13 to 7.

The first loading step for the simulations is to deflect the rod until the free end is at a right angle to the fixed end. Upon the formation of the torus configuration the actuator can be further deformed by external loads. These loads occur due to constraints on the

WSL robot itself and deflections are in fact the natural input to the problem for a collapsed environment. The second loading step for the simulation in Fig. 2.6 is an applied deformation of the quarter model to simulate a constricting force, Q, acting on the ring actuator and causing a deflection.

2.3.1 Ring Stiffness

The theory of rods enables the solution to problems with subsequent deformations. The WSL actuator is a cylindrical rod that is formed into the shape of a torus by bending. The pre-stressed configuration of a ring makes the everting motion possible. In fact, an isotropic ring formed by the bending of a circular cylinder everts with zero force assuming drag and inertia to be zero. This means a pre-stressed ring is an excellent candidate for the WSL actuator which utilizes eversion to generate motion.

The design of the WSL actuators involves several key parameters. One of which is the deflection force, Q, as was described in Section 2.1. This force has been shown to play a role in the ability to deform the WSL robot in order to squeeze through narrow passageways. The required torque and the minimum coefficient of friction have been shown to be proportional to the magnitude of the deflection force, Q (Eq. 2.2).

As the deflection force increases, the required static torque of the actuators and the coefficient of friction, μ must increase to allow passage through a constriction. The deflection force, Q, is related to the bending rigidity of the rod and the extensional stiffness if the rod

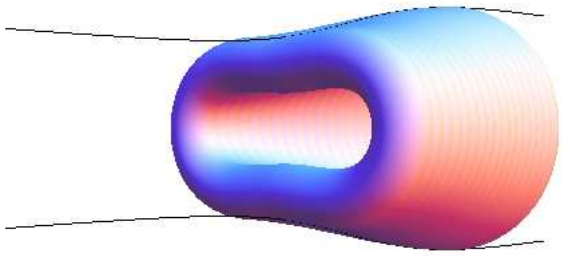

FIGURE 2.7: The WSL deforming in order to squeeze itself into a constricted passageway

is extensible.

Several simulations were conducted by deflecting the pre-formed ring by a pinching load in the vertical direction. The axial curve of the deformed ring is shown in Fig. 2.8. The force-deflection curve calculated for the simulation is shown in Fig. 2.9.

The result of this simulation is telling of a more general design consideration. Since the simulation was performed using nondimensional quantities a wide range of rod properties can be explored by modifying the length and bending stiffness of the rod used to form the actuator. Note that the values obtained in Fig. 2.9 define torque requirements as demonstrated in Eq. 2.2. The quantities in Eq. 2.2 are point wise and for implementation in torque specification the distinction between net torque and pointwise torque must be developed as will be done in Chapter 5.

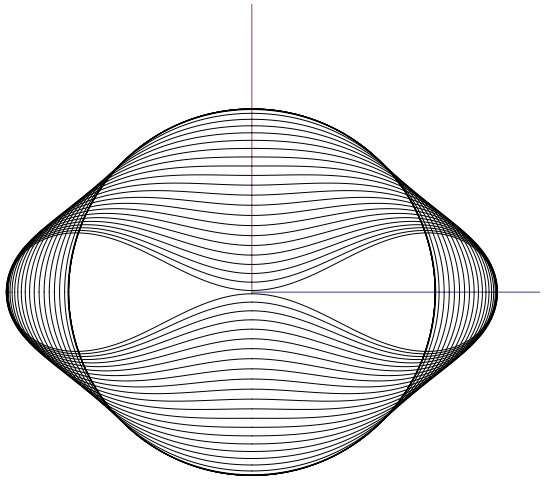

FIGURE 2.8: Subsequent deformations of a ring due to a pinching load

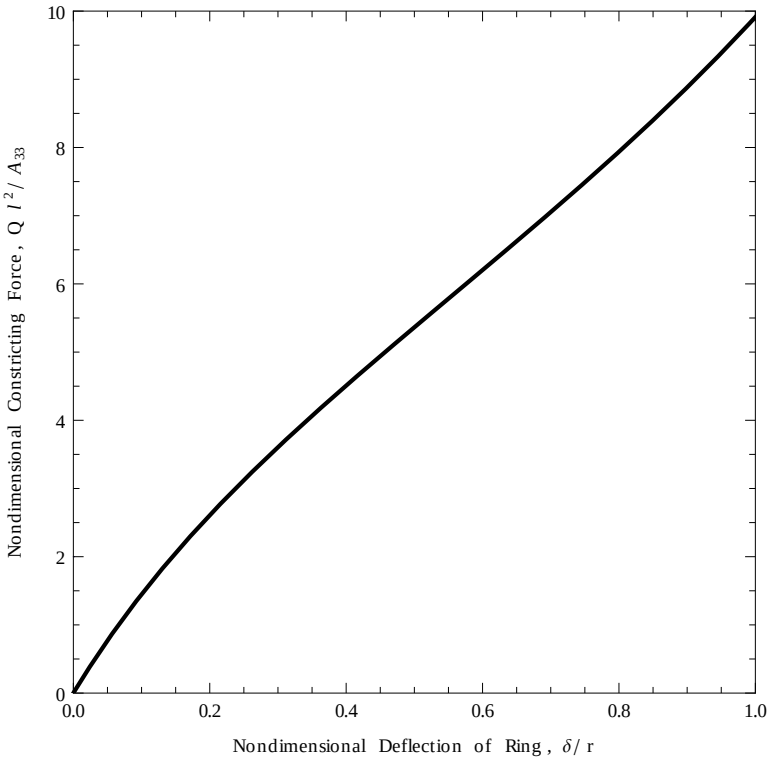

FIGURE 2.9: The force-deflection curve for Fig. 2.8

2.3.2 Everting Rings

As mentioned previously, the everting torque of a ring formed by the bending of an isotropic circular cylindrical rod is zero. It can be further stated that the bending of a linear elastic transversely isotropic circular cylinder will also result in a zero everting torque. What must be demonstrated however is that these examples are ideal and the real torque will be nonzero due to the imperfections in the torus properties.

For instance, the case of a ring formed by the bending of a rod with a non-circular cross section will have a nonzero everting torque. This can be made evident by the change in the second moment of area as the ring everts. Also the case of everting a ring formed by a initially curved rod has nonzero everting torque. The torque will vary sinusoidally as the change in curvature $\vec{æ} - \vec{æ}_0$ varies. This explains why a ring formed without residual stress requires a nonzero everting torque and exhibits a snap through as the everting angle approaches π. An example of such a ring is an o-ring that everts, but has only one stable equilibrium position and exhibits a sinusoidal everting torque when perturbed from rest.

The torque required to evert a ring which has curvature in its stress free reference state can be determined as a function of everting angle. If the ring is planar and has curvature in its reference configuration, $æ_{03}$, then the governing equations are simplified.

If the ring everts due to a uniform constant applied torque, the internal torsion due to

twist is zero. The curvatures in the deformed configuration become

$$\text{æ}_1 = 0 \tag{2.32}$$

$$\text{æ}_2 = \text{æ}_{03}\sin[\theta_1] \tag{2.33}$$

$$\text{æ}_3 = \text{æ}_{03}\cos[\theta_1] \tag{2.34}$$

where θ_1 is the everting angle. The constitutive relations for the nonzero internal bending moments, M_2 and M_3, are

$$M_2 = A_{22}(\text{æ}_{03}\sin[\theta_1]) \tag{2.35}$$

$$M_3 = A_{33}(\text{æ}_{03}\cos[\theta_1] - \text{æ}_{03}) \tag{2.36}$$

The one nontrivial equilibrium equation is the torque balance in the tangent direction $\vec{e}_1$ (Eq. 6.1).

$$M_3\text{æ}_2 - M_2\text{æ}_3 + T_1 = 0 \tag{2.37}$$

The number of equations is equal to the number of unknowns so we can solve for T_1. If the bending stiffnesses A_{22} and A_{33} are distinct then the torque T_1 becomes

$$T_1 = A_{22}\text{æ}_{03}^2\sin[\theta_1]\cos[\theta_1] - A_{33}\text{æ}_{03}^2(\cos[\theta_1] - 1)\sin[\theta_1] \tag{2.38}$$

$$= (A_{22} - A_{33})\text{æ}_{03}^2\sin[\theta_1]\cos[\theta_1] + A_{33}\text{æ}_{03}^2\sin[\theta_1] \tag{2.39}$$

$$= \text{æ}_{03}^2\sin[\theta_1]((A_{22} - A_{33})\cos[\theta_1] + A_{33}). \tag{2.40}$$

For the case when the bending stiffnesses are the same $A_{22} = A_{33} = EI$

$$T_1 = EI\text{æ}_{03}^2\sin[\theta_1]\cos[\theta_1] - EI\text{æ}_{03}^2(\cos[\theta_1] - 1)\sin[\theta_1] \tag{2.41}$$

$$= EI\text{æ}_{03}^2\sin[\theta_1] \tag{2.42}$$

It can be seen that the required torque to evert a ring with initial curvature and zero pre-stress is a function of that initial curvature and the eversion angle. If the initial curvature goes to zero, the torque amplitude to maintain equilibrium under eversion also goes to zero.

Also at $\theta_1 = \pm\pi/2$ a snap through instability occurs and the ring would deform rapidly attempting to return to the stable equilibrium point. The deformation and loads during this instability could be damaging to the structure and should be either accounted for or avoided in the design of such an everting structure.

2.4 Discussion

The examples from this chapter have illustrated components to the modeling effort for the development of the WSL actuators. The analysis of the constriction of the WSL robot due to its own generated forces revealed the connections between the parameters of the model. It was shown that the deflection stiffness, Q, plays a big role in the ability for the robot to overcome obstacles.

The analysis of rings demonstrates the benefits to the WSL robot actuation strategy based on pre-stressed toroidal actuators. This has been demonstrated without reference to the actuation forces and torques specifically as this will be discussed in the next chapter.

Chapter 3

Shape Memory Alloy Composite Rods

3.1 Background

The theory of rods was developed in Chapter 2 such that problems of isotropic rods could be formulated and solved. The rods were acted upon by external forces without a direct explanation of where such forces originate. It is the focus of this chapter to develop the loads which can be produced by a SMA wire onto a composite rod.

The geometry of rods was described using the Darboux frame which is attached to the axial curve of the rod. The deformed configuration is held in equilibrium by external forces which act on the axial curve of the rod.

The case is now introduced in which line loads are offset a vector distance, $\vec{d}$, from the axis of the rod. These loads are due to the SMA wires embedded on the exterior of the rod

and produce a distributed load, P, and a distributed torsional load, T. These distributed loads originate because of the stress in the SMA wires.

The magnitude of distributed load due to a tensile force in an SMA wire can be described using the nonlinear theory of strings [29]. This development will be provided in the following sections.

3.1.1 SMA composite structures

Rod theory has been used for SMA composite structures including studies of composite rod actuators. For example, Lagoudas et al. developed the theory of an inextensible rod actuated by an SMA wire [40]. Turner et al. developed a model for a SMA hybrid composite for vibration suppression [41]. Recently Veeramani et al. developed a SMA active catheter that uses eccentric SMA wires to bend a long tube [42].

To date, much of the research on SMA composite rod structures has made assumptions about the fixity between the wires and the rod structure. These assumptions introduce a constraint between the strain state of the wires and the matrix. The constitutive models proposed by Turner et al. and others have proposed that the stress in the wires can also be "smeared" with the matrix properties such that the net properties are consistent with volumetric averages [25]. This technique is called the rule of mixtures and produces a homogenization of the matrix and fibers [43].

Despite all of the work utilizing these fixity assumptions, it has been shown that there

are finite limits to the shear stress at the fiber matrix interface [44]. To attempt to improve matrix adhesion Jonnalagadda et al. have demonstrated surface treatments for the SMA wire [44].

The use of property averaging constitutive relations are not valid when the fibers in a composite move relative to the matrix. Thus structures utilizing SMA wires which translate relative to the composite must rely on tracking the wire as it moves in the matrix. In our study we have developed a model that tracks the length of each SMA wire as the structure deforms. The length of each SMA wire provides a lumped representation of the SMA wire stress state that can be used with 1D constitutive models to simulate actuation dynamics.

It is not the focus of this work to demonstrate the actuation dynamics, but rather a quasi-static basis for future work in actuator behavior.

3.2 Nonlinear strings

Strings are a specialization of rods without bending rigidity. Also, since the strings are considered thin it is assumed that only body forces can act on the string. Because of this, strings can only support loads tangent to their spatial configuration if body forces are not present. A classic example of this is a string held solely by tension on its two ends; the string is in the configuration of a straight line with a constant tangent vector.

Similar to rods the equilibrium equations for strings are described by ODEs with the arc length, s, as the independent variable. When the string is curved, normal forces must

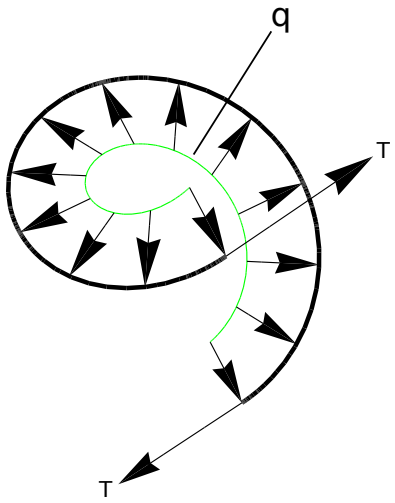

FIGURE 3.1: A nonlinear string supported by normal forces, q, and tensile forces, T

support the tension (Fig. 3.1). The tension vector, $\vec{T}$, is a function of the local arc length coordinate and the equilibrium equation can be written

$$\frac{d\vec{T}}{ds} + \vec{q} = 0 \tag{3.1}$$

where $\vec{T}$ and $\vec{q}$ are the tension vector and the body force vector respectively. The Frenet frame can be used in this development since torsion of the strings is not considered in this case (Eq. 2.9).

For the case of this work, the effect of body forces will be included as they act on the composite rod structure through normal support loads and tangential frictional loads. If a string is supported on a curved surface with known curvature, then the derivative with respect to arc length is expanded to include the effects of normal force resultants (Eqn 3.2).

$$\frac{\breve{d}\vec{N}}{ds} + \vec{\kappa} \text{ x } \vec{N} + \vec{f} = 0 \tag{3.2}$$

The body force, $\vec{f}$, is the resultant of two components; one acting in the normal direction

and the other acting in the tangential direction. The binormal direction is satisfied trivially since no loads are present in that direction. The normal component of force at a point on the string is a function of the curvature. Previously in Chapter 2 a simple relationship between friction and the normal force was developed in Eq. 2.1.

$$\frac{\breve{d}\vec{N}}{ds} = \vec{f_s} = \mu_s \vec{f_N} \tag{3.3}$$

If the effect of friction is neglected ($\mu_s \approx 0$) it can be stated that the local derivative of tension force can be neglected as the force does not change over the length. This requires that the body force be equivalent to the curvature term. Also, a zero frictional force acting on the wire means that the tension of the string is constant.

$$\vec{f} = -\vec{\kappa} \text{ x } \vec{N} \tag{3.4}$$

If however the frictional force cannot be neglected then the tension in the string varies along the length. If the string is a SMA wire then the point of highest frictional force will possibly reach stress levels which may damage the wire so care must be taken to reduce friction when possible. In our problem, the effect of friction is neglected. Additional material coordinates would have to be placed on the string in order to supplement our model with the effect of friction and a more robust interaction would need to be defined.

3.3 String Interaction with Rods

The previous section dealt with the loads on a string in equilibrium. The body forces that were determined from the previous development act on the rod structure and vice versa. Now the coupling is considered more thoroughly by examining the interface geometry between the two bodies. It is assumed that relative motion between the rod and the string may occur, but since the actuators are in the form of a closed loop the bodies always remain in contact.

The arc length parameter for the theory of nonlinear strings is subject to stretch unlike the previous development for rods. This is a necessary complication, since the SMA wire must be strained in order to develop recovery stresses. Since the bonding between the wire and the matrix material of the rod is not assumed to be rigid, the local description of strain differs between the two bodies.

Since the rod can be considered inextensible, it offers a reference for which to determine strain locally (Eq. 2.20). The change in bending curvatures of the rod and the distance between the axis of the rod and the point of interest give a full description of the strain of the rod at a point. These local strains may be integrated at each time step to determine the net stretch in the SMA wires. If the stretch increases with time then the strain must also increase.

In order to simulate the basic behavior of line loads from the SMA wire onto the rod structure the deformed configuration of the wire must be described. Since there are a finite number of SMA wires in the SMA rod, the structure is not considered homogeneous.

Therefore the applied load from each wire onto the structure must be considered separately.

3.3.1 Spatial Configuration of SMA wires within Rod

If the rod is initially straight and the fibers are oriented along the tangent vector to the rod axis, then the position of the string in the reference configuration is described by

$$\vec{p_0} = \vec{r_0} + \vec{d_0} \tag{3.5}$$

where $\vec{r_0}$ and $\vec{d_0}$ are the position of the undeformed axis of the rod and the vector offset of the fiber and the centroid of the rod cross section.

For the case of the initially straight composite rod, the arc length of the fiber in the reference configuration is equal the arc length of the rod. For the case of an initially curved configuration see Lagoudas et al. [40].

The arc length changes upon deformation so the local strain of the fiber is made in reference to the deformed configuration of the rod. The deformed configuration of the fiber can be described by the deformed state of the rod

$$\vec{p} = \vec{r} + \vec{d} \tag{3.6}$$

where the vectors $\vec{r}$ and $\vec{d}$ are the deformed versions of $\vec{r_0}$ and $\vec{d_0}$ from Eq. 3.5. The vectors are described in terms of the attached coordinate system which can be transformed into the fixed cartesian coordinates using the direction cosines, $[L]$, which are described in Eq. 2.5.

The deformed length of the strings can be found by determining the magnitude of the unit tangent vector, $\frac{d\vec{p}}{dz}$, along the string axis.

$$\frac{d\vec{p}}{dz} \cdot \frac{d\vec{p}}{dz} = 1 \tag{3.7}$$

Since the arc length in the deformed configuration is not yet known, the chain rule is used to expand the expression in Eq. 3.7 to the form of Eq. 3.8.

$$\left(\frac{dz}{ds}\right)^2 = \frac{d\vec{p}}{ds} \cdot \frac{d\vec{p}}{ds} \tag{3.8}$$

The vectors are expanded using Eq. 2.11 so that the arc length of the deformed string can be determined in terms of the rod curvatures, $æ_i$, and offset vector components, d_i.

$$\begin{aligned}
\left(\frac{dz}{ds}\right) &= \left(\frac{d\vec{r}}{ds} \cdot \frac{d\vec{r}}{ds} + 2\frac{d\vec{r}}{ds} \cdot \frac{d\vec{d}}{ds} + \frac{d\vec{d}}{ds} \cdot \frac{d\vec{d}}{ds}\right)^{1/2} \\
\left(\frac{dz}{ds}\right) &= \left((1 + æ_3 d_2 - æ_2 d_3)^2 + \left(æ_1 d_3 + \frac{dd_2}{ds}\right)^2 + \left(-æ_1 d_2 + \frac{dd_3}{ds}\right)^2\right)^{1/2}
\end{aligned} \tag{3.9}$$

If the fibers are neither twisted in the reference configuration nor do the offset distances change as a result of deformation then Eq. 3.9 reduces to Eq. 3.10.

$$\left(\frac{dz}{ds}\right) = \left((1 + æ_3 d_2 - æ_2 d_3)^2 + æ_1^2(d_2^2 + d_3^2)\right)^{1/2} \tag{3.10}$$

In addition, if the curvature of torsion, $æ_1$, is considered small, then the rate of change in arclength, $\frac{dz}{ds}$, becomes

$$\left(\frac{dz}{ds}\right) = (1 + æ_3 d_2 - æ_2 d_3). \tag{3.11}$$

Since the description of the axial curve for the string has been determined it is now the task of finding the Frenet frame of the string in the deformed coordinates (Eq. 2.9). This involves computing the tangent vector, normal vector, curvature and torsion of the string's spatial curve.

The unit tangent vector is calculated first as the remaining quantities can be found as a result of its value. It is again assumed that the components of the vector offset, d_i, do not change as a result of deformation. It is a simple task to include the derivatives as in Eq. 3.9, however this will not be done at this time for the sake of simplicity.

$$\vec{t} = \frac{d\vec{p}}{dz} = \frac{d\vec{p}}{ds}\left(\frac{ds}{dz}\right) = \frac{d\vec{p}}{ds}\left(\frac{dz}{ds}\right)^{-1} \tag{3.12}$$

Since $\vec{t}$ is a unit vector, its change with respect arc length, z, is the radius of curvature in the osculating plane [38]. Thus, the curvature of the string axis is calculated by

$$\kappa\vec{n} \cdot \kappa\vec{n} = \kappa^2 = \frac{d\vec{t}}{dz} \cdot \frac{d\vec{t}}{dz}, \tag{3.13}$$

solving for the curvature and using the chain rule we arrive at

$$\kappa = \left(\frac{d\vec{t}}{dz} \cdot \frac{d\vec{t}}{dz}\right)^{1/2} \tag{3.14}$$

The result from Eq. 3.14 demonstrates that the unsigned curvature, κ, can be completely determined by the deformation state in the rod. The sign of curvature is determined by the sign of the the rotation of the tangent as it moves along z.

If the torsional curvature, $æ_1$, is considered small then the curvature of the string reduces

to

$$\kappa = \frac{\sqrt{æ_2^2 + æ_3^2}}{1 + æ_3 d_2 - æ_2 d_3}. \tag{3.15}$$

The unit normal vector is now calculated using the Frenet frame. As in Eq. 3.15 the torsional curvature will be considered small so that Eq. 3.16 reduces complexity significantly.

$$\vec{n} = \frac{1}{\kappa}\frac{d\vec{t}}{dz} = \frac{1}{\kappa}\frac{d\vec{t}}{ds}\left(\frac{dz}{ds}\right)^{-1} \tag{3.16}$$

Following a similar procedure we could calculate the torsion of the string axis, however for the purposes of this work we restrict our focus to the osculating plane ($\vec{t} \times \vec{n}$). Note that the terms which result from Eq. 3.15 and Eq. 3.16 explode without the simplifying assumptions such as small twist and negligible radial expansion of the rod.

3.4 Equilibrium of SMA composite rod actuator

Now the Equilibrium of the SMA composite rod will be explored using the geometric parameters of the string configuration in addition to the equilibrium equations Eq. 3.1. As stated in the previous section, the directions of interest are the normal and tangential directions which both lay in the osculating plane.

The body force vector acting on the string, $\vec{q}$, is of particular interest as these will be the actuation forces on the rod structure.

$$\begin{aligned} \frac{dT}{dz} + q_t &= 0 \\ \kappa T + q_n &= 0 \end{aligned} \tag{3.17}$$

To apply the body forces found from Eq. 3.17 onto the rod structure, we are first required to transform the forces to unit lengths on the rod axis [40].

$$\vec{P} = -\frac{dz}{ds}\vec{q} \tag{3.18}$$

In addition to the forces applied directly to the rod axis, we must also include the effects of torsional loads generated by the wires.

$$\vec{M} = \vec{d} \times \vec{P} = \vec{d} \times -\frac{dz}{ds}\vec{q} = \frac{dz}{ds}\vec{q} \times \vec{d} \tag{3.19}$$

With the equilibrium equations presented for rods (Eq. 2.23) and the distributed loads (Eqs. 3.18 & 3.19) we have a full representation for the equilibrium in the SMA composite structure. The tension in the SMA wire was assumed known but can be explicitly derived with help of constitutive relations for SMA materials. The distributed load from one wire is depicted in Fig. 3.2. Note that the local value of the distributed load is proportional to the net bending curvature of the rod (Eq. 3.20).

$$\vec{M} = \{0, -\kappa T\frac{dz}{ds}, 0\} \times \{0, d_2, d_3\} = -\kappa T\frac{dz}{ds} r\cos\theta \tag{3.20}$$

If the vector offset, $\vec{d}$, of the wire is a constant distance, the applied torque, M, from the wire becomes

$$\vec{M} = -\left(Tr\sqrt{æ_2^2 + æ_3^2}\right)\cos\theta\vec{t} \tag{3.21}$$

where $æ_2$, $æ_3$, r, and θ are the bending curvature components in the two attached coordinates, the radius offset of the wire from the center of the actuator and the angle between the wire position vector and second attached coordinate axis.

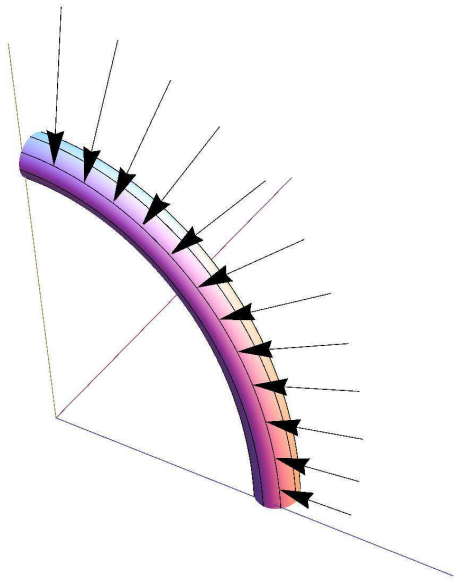

FIGURE 3.2: The distributed load applied to the rod by a tension in one wire

A maximum applied torque from the wire occurs when the attached coordinates are rotated to the direction of principal curvature ($æ_3 = 0$,$æ_2 = \kappa_p$) and the wire is at an angle $\theta = 0$.

$$\vec{M} = (Tr\kappa_p)\,\vec{t} \tag{3.22}$$

Chapter 4

Modeling the Behavior of Helical Springs

The mobility of the robot can be further enhanced by the introduction of an extensible rod support for the actuators. This is especially important in cases where the robot is venturing into a narrow passage which has a perimeter less than that of the actuator perimeter. The inextensible actuator base does not allow passage into such small passageways. In addition the flexibility in the axial direction can alleviate stress in the SMA wires and help avoid overloading.

Springs have been in existence for several centuries and inspired the basis of Hooke's law [45]. For a thorough history and development of the theory of springs see Wahl [46]. In his treatise, Wahl develops nonlinear spring theories and summarizes the development of others

in the text and contains a large bibliography of works in the area.

Timoshenko included a chapter in his seminal work "Strength of Materials" on the development of theories for various loading conditions for open helical springs [47]. Svetlitsky developed a nonlinear theory of helical springs as part of his text on rod theory [33].

4.1 General Helical Springs

In order to model a helical spring as the skeleton of the SMAC actuator we must model the kinematic and kinetic properties of helical springs. For the general case such a model must encompass the range of behavior including deformations with noncontacting and contacting coils. The following development considers a representative model of a helical spring in a homogenized form such that the equilibrium of a one dimensional rod is sufficient to describe this range of behavior.

Helical springs have primarily been considered for providing axial stiffness. The study of helical springs has most often been performed using linearized models which do not consider coil contact or the bending rigidity [48]. The axial and bending properties become coupled when contact occurs. We will consider both loads separately then consider their effects when coupled.

4.1.1 Axial Stiffness

The axial stiffness of a spring can be modeled with various degrees of precision. The axial stiffness utilized for bending of springs is defined by

$$k = \frac{F}{\delta} \tag{4.1}$$

where F and δ are the axial force and deflection of a spring. The deflection, δ, is defined as the total deflection of a spring of given length. This type of stiffness specification is a lumped description in the way that the properties of the spring are taken as a whole over the entire length. For our purposes the spring is to be modeled as a continuum and the stiffness, k, and the deflection, δ are replaced by the stiffness per unit length, k_e, and the strain, e, respectively.

$$k_e = \frac{F}{e} \tag{4.2}$$

The axial stiffness of a helical spring with a rectangular cross section is

$$k_e = \frac{72Ek^2k_1(a_r)}{c^2a_r\left(6k_1(a_r)\alpha + \frac{a_r^2(1+\nu)}{\alpha}\right)} \tag{4.3}$$

where E, k, k_1, a_r, α and ν are the Young's modulus, radius of gyration of the cross section, the shear correction for rectangular cross sections, the ratio of base to height of the cross section, the helix angle and Poisson's ratio respectively. Note that the model is derived based on Dym 2009, but varies distinctly in that it is for a rectangular cross section. The introduction of the radius of gyration and shear correction terms are our contribution to the form of the stiffness Dym developed. Since in general the radius of gyration for a rectangular

cross section can be found for two axes of symmetry the radius of gyration was defined to be

$$k = \sqrt{\frac{I}{A}} = \sqrt{\frac{\frac{16b^3h}{12}}{bh}} = \frac{b}{\sqrt{3}} \tag{4.4}$$

where b, h, I and A are the base of the cross section, the height of the cross section, the moment of inertia of the cross section and the area respectively.

The spring index used in Eq. 4.3 was also defined for a rectangular cross section by first determining the radius of gyration for the cross section (Eq. 4.4) then comparing this radius of spring coil to the radius of gyration, k.

$$c = \frac{R}{k} \tag{4.5}$$

The spring index, c, has a range from 4 to 12 for typical spring applications [48]. Increasing the spring index while keeping the same cross section properties effectively softens the spring in axial load as can be seen from Eq. 4.3. The relative magnitudes of axial, torsion and bending will be developed and it will soon become apparent how the spring index plays a large role in these magnitudes.

When a spring is compressed from its undeformed length the compressive force is proportional to the deflection. At the point when the coils contact each other the spring stiffness increases radically as the material of the coil is now in the form of a hollow cylinder. Since the stiffness at this contact is proportional to the Young's modulus times the area it will be considered infinite compared to the flexible spring. The force over deflection curve for a spring in compression is pictured in Fig. 4.1. This approximates the axial behavior if there

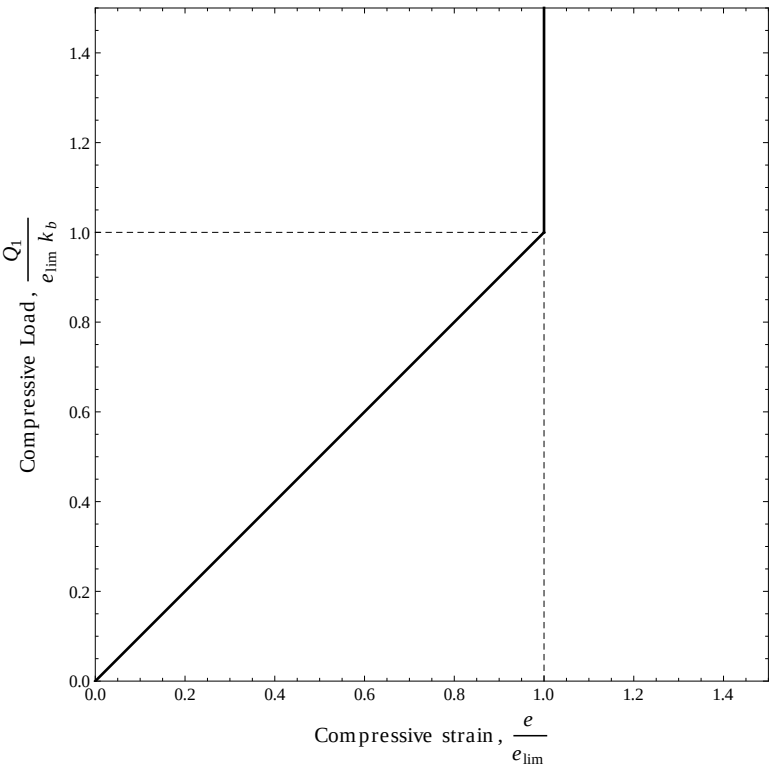

FIGURE 4.1: Compressive axial load versus axial compressive strain

is no curvature in the spring axis.

4.1.2 Bending Stiffness

The bending of an open coiled helical spring prior to coil contact can be described by a linear relationship

$$M = \beta\kappa \tag{4.6}$$

where the bending stiffness, bending moment and curvature are β, M and κ respectively. The bending stiffness, β, has been determined by Timoshenko [47] to be

$$\beta = \frac{sin(\alpha)}{\frac{1}{EI_1} + \frac{sin(\alpha)^2}{EI_2} + \frac{cos(\alpha)^2}{GJ}} \tag{4.7}$$

where the Young's modulus, shear modulus, moment of inertia, polar moment of inertia and helix angle are E, G, I, J and α respectively. The distinction between the two moments of inertia are retained by the terms I_1 and I_2 are for the two axes by which the coil can bend. The depiction of bending stiffness for springs has been developed primarily for springs with circular cross sections where this distinction is not required. The polar moment of inertia, J, for a section must include the aspect of warping if the cross section of the coil is not circular. This involves the shear correction, k_1, which provides a modifier for the torsional rigidity of rectangular cross sections. This shear correction is a function of a_r, the ratio of the base to the height of the cross section.

The shear correction we are using was developed based off of Boresi's derivation (Eq.

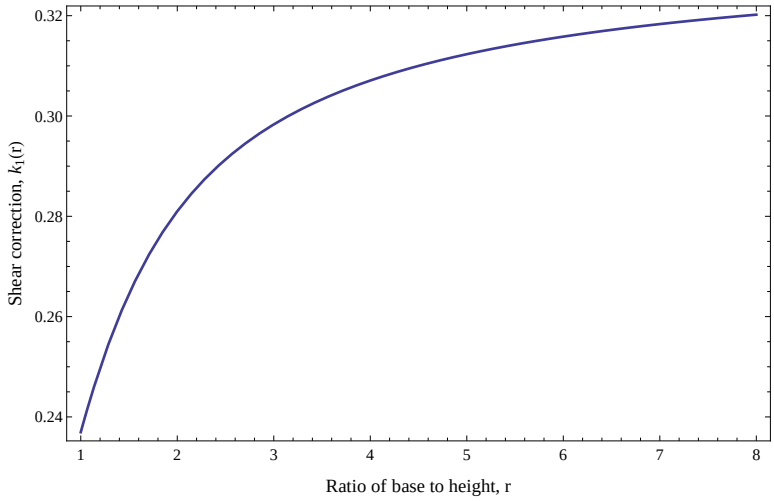

FIGURE 4.2: Shear correction for torsion of rectangular prisms

4.8) [49]. The shear correction factor is

$$k_1 = \frac{1}{3}\left(1 - \frac{192}{\pi^5 a_r}\sum_{n=1}^{\infty}\frac{\tanh\left(\frac{1}{2}\pi(2n-1)a_r\right)}{(2n-1)^5}\right) \tag{4.8}$$

where r is the ratio of the base, b, over the height, h, of the cross section. A graph of the magnitude of the shear correction as a function of the ratio of base to height, r, is displayed in Fig. 4.2. Note that as the aspect ratio increases the shear correction reaches an asymptote of the thin section approximation [49].

The situation for bending stiffness for a rectangular cross section is rather complicated since there is additional information such as the aspect ratio of the cross section and the effect of torsion of a non-circular section does not allow for the same simplifications. Utilizing the aspect ratio, the shear correction and radius of gyration the bending stiffness of a spring with a rectangular cross section can be found (Eq. 4.9).

$$\beta = \frac{144Ek^4k_1\sin(\alpha)}{6k_1a_r\left(a_r^2\sin^2(\alpha)+1\right)+(\nu+1)a_r^3\cos^2(\alpha)} \tag{4.9}$$

The simplification for small helix angles can be made for $\alpha < 10^o$. The corresponding simplification produces a bending stiffness of

$$\beta = \frac{144Ek^4\alpha k_1}{6k_1 a_r + (1+\nu)a_r^3}. \tag{4.10}$$

Considering the much simpler bending stiffness for a spring with a circular cross section involves the simplifications of $J = 2I$ and $G = \frac{E}{2(1+\nu)}$. Note that linear elastic properties have been assumed. Upon these substitutions and with further simplification we can see that

$$\beta = \frac{2EI\sin\alpha}{1+\sin^2\alpha+(1+\nu)\cos^2\alpha}. \tag{4.11}$$

For the case where α is considered small ($\alpha < \frac{\pi}{9}$) the result from Eq. 4.11 can be further simplified to

$$\beta = \frac{2EI\alpha}{2+\nu} = \frac{\pi\alpha Er^4}{2(2+\nu)} \tag{4.12}$$

4.1.3 Torsional Rigidity

In the previous development of contact conditions and the effect of contact on the bending and axial stiffnesses we did not consider torsion. Torsion is not affected directly by contact of coils for the design range of the SMAC. Similar to the development of axial strain we seek to put torsion given in the form

$$k_t = \frac{T}{\phi} \tag{4.13}$$

where the torsional stiffness, torque and twist between two points on the spring are k_t, T and ϕ respectively. This torsional rigidity is the traditionally used value for spring with a

finite predetermined length. Since we seek to model the spring as a continuum we require a stiffness per unit length.

The torsional stiffness for a spring with a rectangular cross section was determined following Dym's derivation, but with the twist that the cross section is rectangular. In addition to this derivation we have incorporated the radius of gyration, k, and the ratio of the cross section, r, as a convenience for later calculations. The torsional rigidity is

$$k_t = \frac{144Ek^4k_1(r)}{\frac{6k_1(r)r}{\alpha} + r^3\alpha(1+\nu)} \tag{4.14}$$

where E, k, k_1, α and ν are the Young's modulus, radius of gyration of the cross section, the shear correction for torsion of rectangular sections, the helix angle and Poisson's ratio for the material.

4.2 General Helical Springs with Contact

As shown previously the contact of coils dramatically changes the behavior of a helical spring. The use of springs as flexible joints or transmission devices must consider the possibility of contact as the loading conditions change. The application of springs for compliant joints was demonstrated by Lotti et al. [17][18] and further analysis was developed by Reggiani in her dissertation [19]. Their focus was limited to that of extension springs with circular cross sections which limits the application of their research to our model and development.

In our work we begin with a general spring that can be either an extension or compression

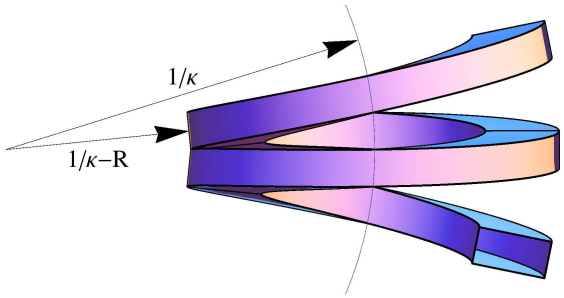

FIGURE 4.3: Rectangular cross section spring with coil contact

spring with either circular or rectangular geometry. This expands the current research in the field in at least two different ways: firstly, we develop a contact condition and subsequent constitutive relations that couple bending and extension; secondly, it develops a model which allows a continuum representation that is not limited to basic mode shapes like other models.

4.2.1 Contact between coils with a rectangular spring

A spring is assumed to bend with the bending stiffness, β, until the coils come into contact. The point of contact can be determined from the geometry of the spring and differs between a circular cross section and a rectangular cross section. Coil contact of a spring with a rectangular cross section can be seen in Fig. 4.3. Also the coil contact of a spring with a circular cross section can be seen in Fig. 4.6.

When a spring with a rectangular cross section is bent to the point of contact it begins to stretch along its axis and changes the effective curvature of the spring. In Fig. 4.3 there is a triangle formed between the center of curvature, the point of contact and the center of the coil. A picture of this triangle is shown in Fig. 4.4.

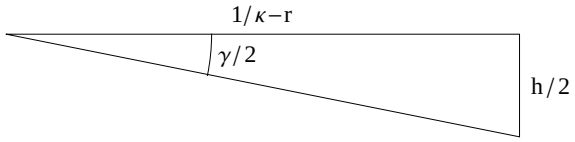

FIGURE 4.4: Contact geometry for a rectangular cross section

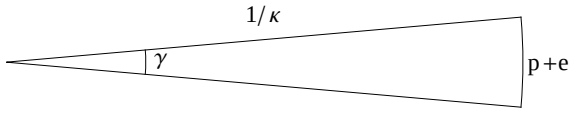

FIGURE 4.5: The arc of one pitch of a spring in contact with itself

The geometry presented in Fig. 4.4 helps to formulate a relationship between the deformation variables. Fig. 4.5 demonstrates the general relationship between curvature, the contact angle and the arc segment of one period of the spring. Note that the absolute value of curvature is used in the equations so that we do not preclude the case where curvature causes extension.

$$\gamma = \frac{p(1+e)}{1/|\kappa|} \tag{4.15}$$

Using the both Eq. 4.15 and Fig. 4.4 the following relationship can be established

$$\tan\left(\frac{p(1+e)}{2/|\kappa|}\right) = \frac{h/2}{1/|\kappa| - r} \tag{4.16}$$

Eq. 4.18 allows for solution for the minimum strain, e_{min}, which is

$$e_{min} = \frac{2}{|\kappa|p}\tan^{-1}\left(\frac{h/2}{1/|\kappa| - r}\right) - 1. \tag{4.17}$$

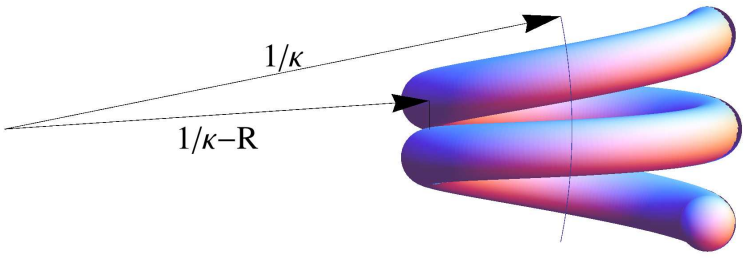

FIGURE 4.6: Coil contact for circular helical spring

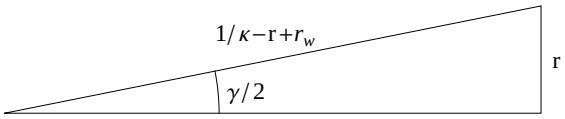

FIGURE 4.7: Contact geometry for a circular cross section

4.2.2 Contact between coils with a circular spring

The minimum extension for a circular cross section helical spring can be found in a similar manner to the previous development for a rectangular cross section spring. Fig. 4.6 illustrates a case where a spring with a circular cross section is bent until self contact.

Similar to the case for a rectangular spring, Eq. 4.15 and Fig. 4.7 may be used to develop the relation for the minimum extension for a spring with a circular cross section.

$$\sin\left(\frac{p(1+e)}{2/\kappa}\right) = \frac{r_w}{\frac{1}{\kappa} - r + r_w} \tag{4.18}$$

The minimum extension for a spring with a circular cross section is determined to be

$$e_{min} = \frac{2}{|\kappa| p} \sin^{-1}\left(\frac{r_w}{\frac{1}{|\kappa|} - r + r_w}\right) - 1 \tag{4.19}$$

where the curvature, cross section height, outer radius and pitch of the spring are κ, h, r and p respectively.

4.2.3 Approximations for a Helical Spring in Contact

For both springs with circular and rectangular cross sections the design range of the geometry will likely allow an approximation for small angles of curvature, γ. Since the radius of curvature is likely to be very large as compared to the outer radius of the spring we may simplify the results for minimum extension by using the small angle approximation for $atan(x) = asin(x) = x$. This approximation is deemed valid for springs with $x < 15^o$, but a full nonlinear solution can be achieved this approximation is not necessary for the development, but convenient for demonstrating the significance of the results. After applying this simplification we arrive at a minimum extension of

$$e_{min} = \frac{2}{|\kappa| p} \left(\frac{h/2}{|\frac{1}{\kappa}| - r} \right) - 1 = \frac{h/p}{1 - |\kappa| r} - 1. \tag{4.20}$$

Note that because the small angle approximation is considered valid, a rectangular cross section (Fig. 4.3) and a circular cross section (Fig. 4.6) have approximately the same minimum extension for a given curvature. This is due to the ratio of the wire's radius relative to the radius of the spring itself. Since the radius of the wire is much less than the spring it is likely that it can be ignored as an approximation. The result of Eq. 4.20 is valid for both an open coiled and a closed coil spring if the height is substituted for the wire diameter, d_w.

Another important point is that the results for the minimum extension are also valid for a closed coil spring where the height of the cross section, h, is equal to the pitch of the spring. This means that contact is present for all ranges of curvatures unless the spring is stretched beyond the minimum by a tensile load.

Axial compression and bending of a spring are coupled when both modes of deformation occur simultaneously. For instance, when a spring is bent then compressed or vice versa, the interaction of the coils causes a coupling between the behavior of the spring in bending and in compression. It should be stated that if the spring is bent and extended there is no such coupling as the extension force does not interact with the bending moment on the spring. The rate of stiffness of the spring in bending or compression becomes discontinuous at the point of contact as the two stiffnesses begin to couple.

If we view the axial compression from the perspective of deflection we see that the compressive stiffness changes from being proportional to the axial load applied to being proportional to the deflection limit which is a function of the curvature. The rate of compressive strain before coil contact is

$$\frac{de}{ds} = \frac{1}{k_e}\frac{dQ_1}{ds} \tag{4.21}$$

and the rate of axial strain during contact is

$$\frac{de}{ds} = \frac{de_{lim}}{ds} = \frac{de_{lim}}{d\kappa}\frac{d\kappa}{dM}\frac{dM}{ds} \tag{4.22}$$

where the chain rule has been applied to simplify the derivative of the limit. The derivative of curvature, κ, with respect to bending moment, M, is found from the constitutive equation for bending moment during contact. The derivative of moment, M, with respect to arc length is defined by the equilibrium equation.

Note that the change in the strain rate causes a piecewise continuous change in the strain in the spring. This change in the rate of axial strain occurs where the state of contact

changes.

For an open coil spring the event of contact must be monitored throughout the entire simulation. This means that Eq. 4.21 must be used if no contact occurs and that Eq. 4.22 must be in the event of contact. This requires that the solution of the combined load problem requires monitoring of a contact condition to ensure that the behavior corresponds with the appropriate case. Note that this contact condition must be checked for the whole domain of the problem and contact may occur in some regions of the spring and not in others.

The contact condition cannot be determined by the strain parameter of Eq. 4.20 (Fig. 4.1) because compression beyond the strain limit is restricted. To circumvent this issue we develop a force parameter which can determine contact without violating this restriction. The contact condition is determined by comparing the axial load to the axial load required to compress the spring to the point of contact. Contact may be monitored by a binary contact condition

$$Q_1 < e_{lim} k_e \tag{4.23}$$

where the compressive load, strain limit and axial stiffness are Q_1, e_{lim} and k_e respectively. The inequality in Eq. 4.23 produces a binary value of TRUE (1) if the compressive stress would produce a contact and FALSE (0) if there is no contact. Eq. 4.23 is immediately useful in switching between the two strain rate relations established in Eqs. 4.21 and 4.22. If contact occurs then the rate of axial strain is confined to the rate defined in Eq. 4.22. If no contact occurs the rate of axial strain is confined to the rate defined in Eq. 4.21.

The development just made for the contact condition and its effect on the constitutive

behavior of axial strain can also be extended to the bending of a spring and the contact condition can be used to develop similar relations. The bending stiffness defined in Eq. 4.6 is valid for cases when contact does not occur (Eq. 4.23=0), but must be adjusted for the case when contact does occur (Eq. 4.23=1).

As the axial strain behavior changed as a result of contact, the curvature is affected by the compressive load at contact. Upon contact between coils the moment required to sustain a value of curvature is increased by the net compressive load acting to compress the coils and thus straighten out the bent spring. The relation in Eq. 4.6 must be adjusted at the point of contact to be

$$M = \beta\kappa + e_{lim}k_e r = \beta\kappa + \left(\frac{h}{1-|\kappa|r} - p\right)k_e r \tag{4.24}$$

The relation derived in Eq. 4.24 can be rearranged to determine the curvature in terms of the stiffness parameters and the applied moment. Note that this relation is only utilized when the contact condition is met (Eq. 4.23=1), otherwise the curvature is directly determined by the moment alone.

The curvature in a contact region is determined by first substituting e_{lim} with its corresponding function of κ (Eq. 4.20). During the solution for κ in terms of the moment, M, it was assumed that the radius of curvature be greater than the radius of the spring. Also it was assumed that the sign of curvature coincides with the sign of bending moment which made it possible to filter the four possible solutions for curvature.

In order to retain the correct magnitude and sign of the curvature, absolute values are

used for the bending moment in the magnitude portion and a sign function is added to distinguish positive and negative curvatures.

$$\kappa = \frac{M}{|M|}\left(\frac{1}{2}\left(1+|M|+2k_e\pi\alpha - \sqrt{(1+|M|+2k_e\pi\alpha)^2 - 4(|M|+2k_e\pi\alpha(1-h/p))}\right)\right) \tag{4.25}$$

In order to express the curvature in terms of a rate form such that the piecewise continuous nature of the curvature itself be retained we take derivatives of Eqs. 4.6 and 4.25 with respect to the arc length. The rate of curvature in a region without contact is

$$\frac{d\kappa}{ds} = \frac{1}{\beta}\frac{dM}{ds} \tag{4.26}$$

The rate of curvature in a contact region is

$$\frac{d\kappa}{ds} = \frac{d\kappa}{dM}\frac{dM}{ds}. \tag{4.27}$$

The contact condition is applied to each term that depends on it. The rate form of the axial force, Q_1, and the bending moment, M, are determined by the solution of the equilibrium equations and the rate of axial strain during contact is defined in Eq. 4.2.

4.2.4 Relative Stiffness for Nondimensional Simulations

The stiffness terms for axial, bending and torsion of a helical spring have been developed in order to quantify the behavior for each individual component. The relative magnitudes of these components are of utmost importance to simplify the modeling and design and provide the basis for a nondimensional representation.

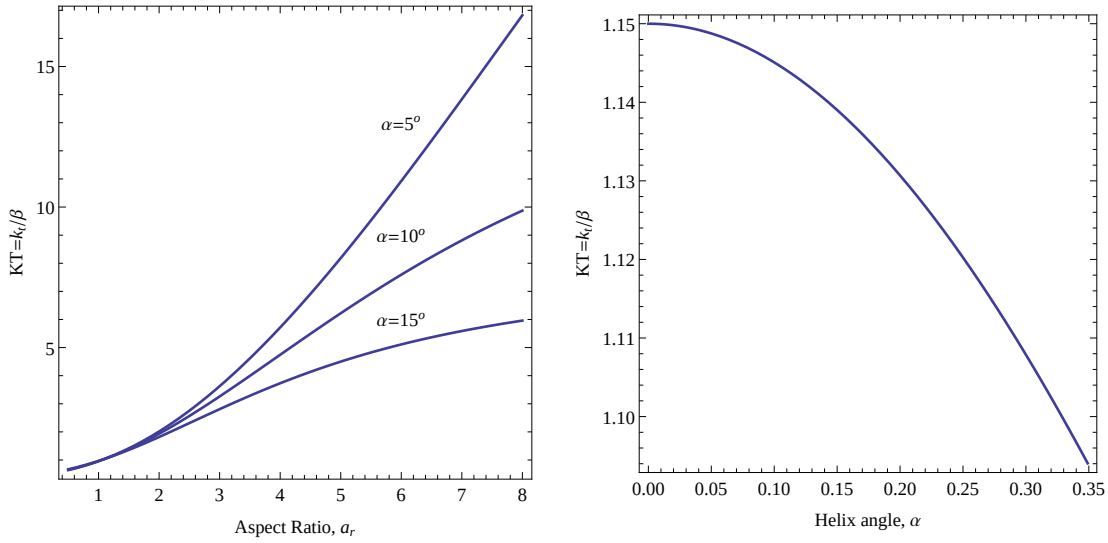

FIGURE 4.8: Ratio of torsional to bending stiffness for rectangular and circular springs

Since the behavior of a helical spring involves bending, torsion and axial stiffnesses we would like to simplify the representation by determining the ratios of these properties for both nondimensionalization and for relative effect on the design of the backbone for the SMAC.

Note that for a dimensionless simulation the forces and moments will be scaled by the bending rigidity and particular attention will be placed on the ratio of the cross section and the radius of gyration as this variable has the strongest effect on the relative stiffnesses of axial/bending. And only the ratio of the cross section varies the torsion/bending ratio.

The torsion/bending rigidity ratio is shown graphically in Fig. 4.8 for a Poisson's ratio of 0.3 and a range of helix angles. Also the axial/bending rigidity ratio is presented in Fig. 4.9 for the same range of Poisson's ratio and helix angles.

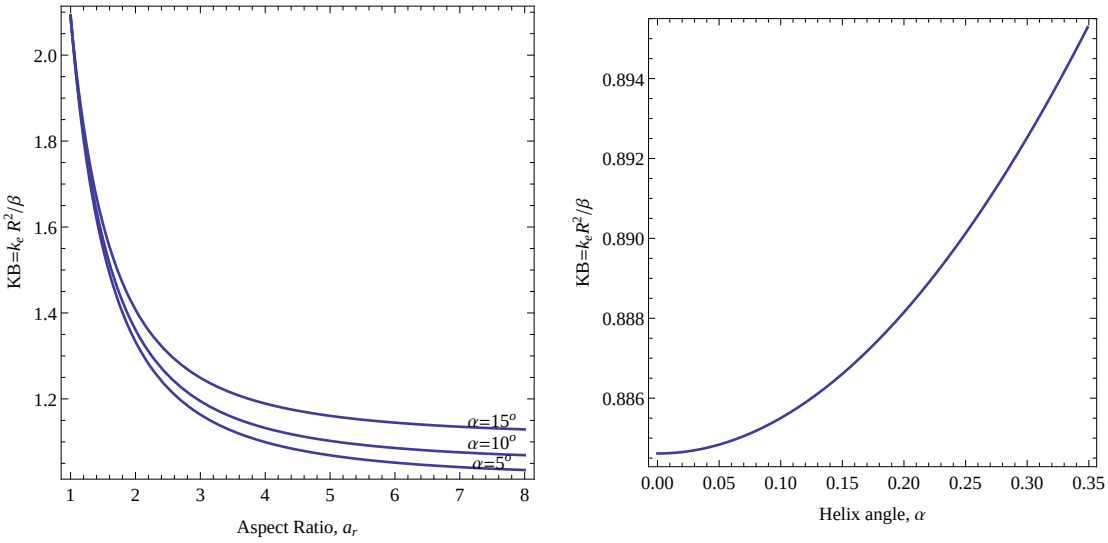

FIGURE 4.9: Ratio of axial to bending stiffness for rectangular and circular springs

The effect of relative stiffness can be demonstrated by looking at a simple case when both the moment and extension are necessary. The first case we will demonstrate is the continuous loading of an open coiled spring from zero curvature through the allowable range for curvature, which is limited to the inverse of the outer radius of the spring. In order to plot this effect we seek a nondimensional representation of the axial/bending coupling.

To develop a nondimensional version of Eq. 4.24 we choose the outer radius, r_0, and the bending stiffness, β, to define a nondimensional moment. Also as noted we need to develop a nondimensional curvature as well, which will be simply $\tilde{\kappa} = \kappa r_0$. Also we assume for the moment that no axial load is present, so we set

$$\tilde{M} = \frac{M r_0}{\beta} = \tilde{\kappa} + e_{lim} \frac{k_e r_0^2}{\beta} \tag{4.28}$$

Upon substitution of e_{lim} and noting our nondimensional ratio of axial/bending stiffnesses

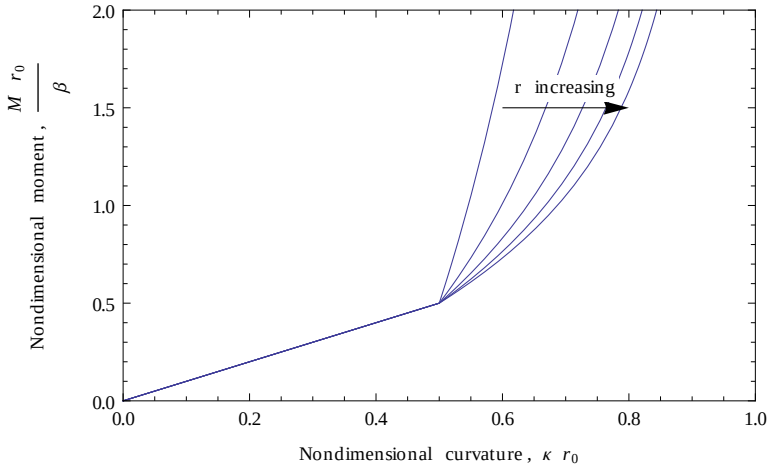

FIGURE 4.10: Bending moment versus curvature ($\alpha = 5^o, \nu = 0.3, h/p = 0.5$)

$\frac{k_e r_0^2}{\beta}$ we can plot the nondimensional moment versus the nondimensional curvature as in Fig. 4.10.

The nondimensional representation for the contact condition in Fig. 4.10 shows the behavior for many different sets of geometry and physical properties. For the following development all forces and moments will be considered in their nondimensional form and the tildes will be dropped, but their sense remains. As depicted in Fig. 4.10 the effect of changing the ratio of base to height of the cross section changes the ratio of axial/bending rigidities.

The curvature as depicted in Fig. 4.10 becomes a piecewise continuous function which has a discontinuity in slope at the nondimensional curvature equal to the height to pitch ratio, h/p. This ratio determines the contact condition for bending and upon manipulation of Eq. 4.28 the curvature can be determined as a function of the bending moment. This

curvature function after contact occurs is

$$\kappa = \frac{1}{2}\left(1 + |M| + 2\ k_b\ \pi\ \alpha - \sqrt{(1 + |M| + 2k_b\ \pi\ \alpha)^2 - 4(|M| + 2k_b\ \pi\ \alpha\ \ (1 - h/p)}\right)\left(\frac{M}{|M|}\right) \tag{4.29}$$

where the geometry constant k_b was added to replace $\frac{k_e r_0^2}{\beta}$ and simplify this expression. Note that for the noncontacting region, the curvature is equal to the nondimensional bending moment, M.

The curvature is an important input in the solution of the equilibrium equations in the attached frame of reference. The curvature is present in many of the equations and thus should be included as one of the dependent variables in the system of differential equations. It acts to deliver force and moment from the wires within the composite and is used to determine the strain in the wires.

Also the contact between coils can be used to stiffen the structure upon reaching a design limit. Essentially the increase in stiffness during contact can be a way to protect the SMA wires from being strained beyond their limits.

4.3 Simulation of helical spring contact with ring deformation

The study of spring properties conducted in the previous sections can be utilized to generate simulation results which are of particular interest in the functional design for the actuators.

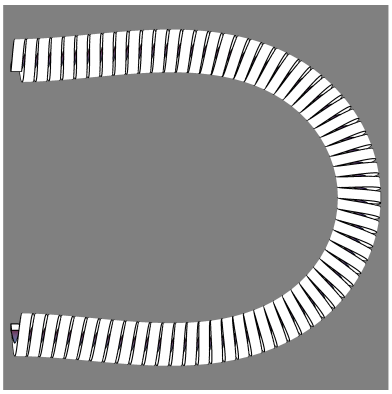

FIGURE 4.11: A helical spring bent from a semicircle to simulate contact force, Q

In order to demonstrate simulation results the nondimensional forms of the equations were utilized to cover a wider range of simulation data. The relative stiffness that was determined earlier between axial, bending and torsional stresses will be used to determine the effects of these quantities on the ring stiffness.

The first type of simulation considered was ring deformation simulations as shown in Fig. 2.8, but with homogenized helical springs as developed in the previous sections.

4.3.1 Ring deformation simulations

The importance of the contact force, Q, was first demonstrated in Chapter 2 and will be emphasized here again. This is the force that the structure generates as it is deformed into constricted spaces. The contact force must be kept small to reduce the load requirement from the actuators. An example of a simulation result is depicted in Fig. 4.11.

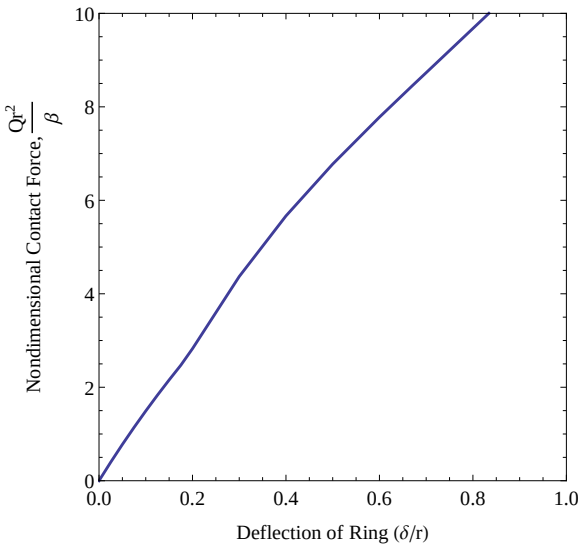

FIGURE 4.12: Contact force generated as the ring depicted in Fig. 4.11 was deformed

Chapter 5

Design of Helical Springs for SMAC

The previous chapter laid out aspects of the behavior of helical springs that relate to the operation and deformation requirements of the actuators. Also simplifying assumptions were made and the homogenization of helical springs was performed such that an approximate model for a rod or beam like representation can be used. The variety of inputs have been discussed and it is now the goal of this chapter to outline a potential design procedure such that structures utilizing helical springs as rods can be optimized.

The benefits of helical springs over that of tubes or solid cylinders is their relative flexibility in various directions. The previous chapter displayed the benefit of rectangular cross section springs and their ability to vary the stiffness components of the spring relative to the bending stiffness. The bending stiffness is of particular interest and the axial and torsional stiffnesses were cast into nondimensional forms to allow for a sensitivity analysis to be com-

pleted. This analysis included the ring stiffness and thrust calculations such that a sense of the design based on these relative stiffnesses could be performed.

5.1 Functional design of actuator

For a consistent operation under various conditions the SMAC actuator must provide adequate thrust force to achieve obstacles. The thrust force comes from the transmitted torsion developed in the actuators and acts to move the robot forward while everting. The actuators produce a torque per unit length as shown in Eq. 3.20.

SMA wires require adequate pre-strain to function as actuators. The risk of too much flexibility either in compression or in bending is that the wires may not retain the ability to actuate. This situation can be remedied as long as the robot is sufficiently stiff in compression and the ring is supported from drastic out of plane motion. Another option is that the torsional rigidity is decreased relative so that the wires will be able to twist the actuators locally. But since this study is limited to actuator design the supporting structure will be considered adequate to these ends and be investigated in greater detail in the future works.

5.1.1 Actuator force requirements

As presented in Chapter 2 the force and torque can be determined for passage into a constriction by the static force balance in Eq. 2.2. The relationship between the thrust force,

P, contact force, Q and the torque, T are shown in the free body diagram in Fig. 2.2.

For small deflections of the torus it can be approximated that the contact force, Q, is linearly proportional to deflection Fig. 2.9. In Fig. 2.9 the contact force is determined for an inextensible rod formed into a ring.

The torque requirement as stated in Eq. 2.2 is true regardless of the level of complexity for the definition of the contact force. Basically this means that the actuator force requirement can be simply expressed as a function of the deformation and tension in the SMA wire. Since the SMA wire exerts distributed load onto the rod proportional to curvature and tension the larger the curvature the larger the distributed load (Eq. 3.19). The wire distributed load can affect the out of plane motion of the ring due to the torsion being converted to bending moment and should be considered when supporting the ring actuators in the shell of the robot.

For the case of one actuator acting alone, this distributed torque can achieve obstacles which have an effective distributed constraint force as depicted in Eq. 2.2. For the case of constraint where contact occurs along a small portion of the actuator the collection of distributed torque applied by the wires acts to overcome the net effect of constraining force, Q. Combining the result from Eq. 2.2 and Eq. 6.21 we arrive at the following integral requirement for torque

$$\int_0^1 (T_1)\, ds > Qr \sin\beta. \tag{5.1}$$

Note that Eq. 5.1 is stated such that the net applied torque is specified as an inequality

which includes the constricting force, Q, and the angle of constriction, β.

5.2 Stress in helical springs

The stress experienced in a helical spring is somewhat complicated. For example, in a spring in compression the cross section experiences torsion and slight bending. When a spring is bent the spring develops a nonhomogeneous stress state and the cross sectional representation must consider various critical points. The state of stress in a helical spring in bending has components due to torsion of the cross section and bending of the cross section. Upon torsion a helical spring's cross section exhibits bending stresses. In combined loading such as bending and axial compression, a spring develops a combination of stress from each loading and has components of bending and torsion of the cross section.

Since the initial properties of helical springs were developed for axial loading the literature does not have many instances of analyses where the loading differs from a pure axial condition. There have been models developed for garter springs which are essentially helical springs which have been formed into the shape of a torus similar to the design we have set out to achieve. However, garter springs were developed for the radial compression or expansion of circular parts such as gaskets or other types of seals [50].

5.2.1 Stresses due to axial load

As mentioned previously, the stress in a helical spring in compression or extension is approximated as the torsion of the cross section. Additional terms like bending, direct shear and axial load can all be considered negligible for small helix angles when the spring is in axial compression or extension.

Circular cross section

The stress from axial load in a spring with a circular cross section is essentially the shear stress due to torsion. The derivation of this stress can be found throughout literature as it is a very well known formula in mechanical design [48]. The maximum shear stress is distributed uniformly on the exterior of the cross section for a circular cross section.

$$\tau_{max} = \frac{Tr}{J} = \frac{(FR\cos\alpha)r}{\pi/2r^4} = \frac{2FR\cos\alpha}{\pi r^3} \approx \frac{2FR}{\pi r^3} \tag{5.2}$$

Rectangular cross section

In a spring with a rectangular cross section the situation is a bit more complicated due to the development of warping in the cross section when torsion is applied. The stress in a rectangular rod in torsion is not uniform as in the circular cross section case. The stress state can be found using the Prandtl membrane analogy for the stress. The shear stress amplitude does not have a closed form solution, but rather a infinite series representation

for the two in plane shear stresses [49].

$$k_0(a_r) = 1 - \frac{8}{\pi^2}\sum_{n=1}^{\infty}\left[(2n-1)^2\cosh\left(\frac{n\pi a_r}{2}\right)\right]^{-1} \tag{5.3}$$

$$k_1(a_r) = \frac{1}{3}\left[1 - \frac{192}{\pi^5}\sum_{n=1}^{\infty}(2n-1)^{-5}\tanh\left(\frac{n\pi a_r}{2}\right)\right] \tag{5.4}$$

Similar to circular cross sections, the shear stresses are maximized at the exterior of the rectangle, particularly at the intersections with the 2 axes of symmetry. The maximum shear stress is found on the narrower of the two sides of the rectangle. In our case in particular, the top of the coil is the point of maximum shear stress since the base is assumed to be larger than the height. The maximum shear stress is

$$\tau_{max} = 2G\theta h\, k_0(a_r) \tag{5.5}$$

where G is the shear modulus, θ is the twist per unit length, h is the height of the cross section and k is an infinite series approximation for the stress function at the critical point [49]. Boresi has defined the twist per unit length as

$$\theta = \frac{T}{G\, k_1(a_r)\,(2h)^3(2b)}. \tag{5.6}$$

Combining the two equations Eqs. 5.5 and 5.6 we can determine the maximum shear stress in terms of the axial load.

$$\tau_{max} = \frac{T}{8bh^2\, k_2(a_r)} = \frac{FR}{8bh^2\, k_2(a_r)} = \frac{\sqrt{3}FRa_r^2}{576k^3\, k_2(a_r)} \tag{5.7}$$

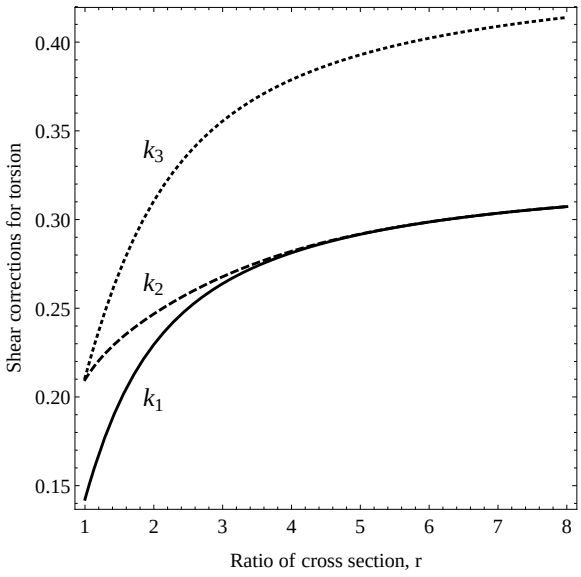

FIGURE 5.1: The shear correction factors for torsion versus aspect ratio

In Eq. 5.7 we have introduced the max shear correction factor, $k_2(a_r)$, which takes into account the k_1/k_0 term that would otherwise be cumbersome. The definition of k_2 is

$$k_2(a_r) = \frac{k_1(a_r)}{k_0(a_r)} = \frac{1 - \frac{192}{\pi^5 a_r}\sum_{n=1}^{\infty}(2n-1)^{-5}\tanh\left(\frac{\pi}{2}(2n-1)a_r\right)}{3\left(1 - \frac{8}{\pi^2}\sum_{n=1}^{\infty}(2n-1)^{-5}\cosh\left(\frac{\pi}{2}(2n-1)a_r\right)^{-1}\right)} \tag{5.8}$$

and a plot showing the magnitude of k_2 for a range of aspect ratios is shown in Fig. 5.1.

5.2.2 Stresses due to bending

The stress state in a spring due to bending can be described by the loads which were utilized in the derivation of bending stiffness [47]. From Fig. 5.2 the two components of bending moment in the plane normal to the axis of the spring.

The applied bending moment on the spring generates three components in an arbitrary

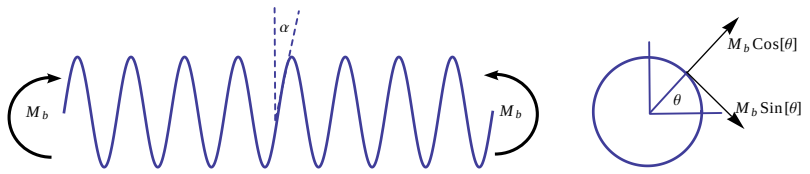

FIGURE 5.2: Pure bending of a spring in its axial plane

cross section of the spring's wire. The three components are torsion about in the direction tangent to the wire and two bending components about the normal and binormal of the wire of the spring. For details of the unit tangent, unit normal and unit binormal vectors of a helix see Kreyszig [37].

The loads generated by a bending moment M applied to a spring are

$$M_t = M \sin\theta \cos\alpha \tag{5.9}$$

$$M_n = M \cos\theta \tag{5.10}$$

$$M_b = M \sin\theta \sin\alpha. \tag{5.11}$$

The three moments are the result of stress in the spring and the maximum stress magnitudes can then be determined by equations that are found in any strength of materials [49] or mechanical design text [48].

Circular cross section

When the spring has a circular cross section we can determine the critical cross section and develop limits to the deformation as was done with axial loads in the previous section. Upon

substituting the bending stiffness from Eq. 4.10 we can determine the stress components for a given curvature. The normal stress due to bending is maximized when $\theta = 0$.

$$\sigma_{tt} = M_b \left(\frac{y}{I}\right) = \beta\kappa \left(\frac{r}{I}\right) = \left(\frac{2Er\sin\alpha}{1+\sin^2\alpha+(1+\nu)\cos^2\alpha}\right)\kappa \approx \left(\frac{2E\alpha r}{2+\nu}\right)\kappa \tag{5.12}$$

The max shear stress that is generated from the torsion of the cross section achieves a maximum at $\theta = 90^o$. The shear stress is

$$\tau_{max} = \frac{(M_t)r}{J} = \frac{(\beta\kappa)r}{2I} = \frac{(\frac{2EI\alpha}{2+\nu}\kappa)r}{2I} = \left(\frac{E\alpha r}{2+\nu}\right)\kappa \tag{5.13}$$

Rectangular cross section

The stress components for a spring with a rectangular cross section in bending are much more complex than for the axial loading case. These complexities arise for a spring with a rectangular cross section due to the mixing of terms in the bending stiffness. In order to express the maximum normal stress we must utilize at least two of the series functions we defined previously. The normal stress due to bending about the binormal axis of the spring at $\theta = 0^o$ is

$$\sigma_{tt} = \frac{-M_b y}{I_b} = \left(\frac{\beta b}{I_b}\right)\kappa = \left(\frac{12\sqrt{3}\alpha E\, k\, k_1}{6k_1+(1+\nu)a_r^2}\right)\kappa. \tag{5.14}$$

And unlike axial loading of the spring we have two different bending moment terms we must consider. The binormal axis above seems to be the likely choice upon inspection, but the normal axis of the spring must be considered as the cross section is not doubly symmetric (Fig. 5.3). The normal stress due to bending about the normal axis of the spring at $\theta = 90^o$

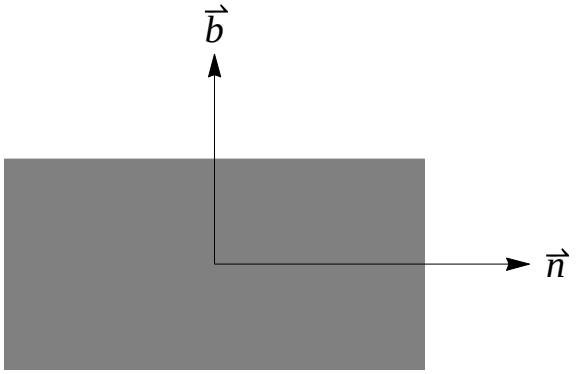

FIGURE 5.3: Cross section of spring showing normal and binormal directions

is

$$\sigma_{tt} = \frac{M_n y}{I_n} = \left(\frac{\beta\alpha h}{I_n}\right)\kappa = \left(\frac{12\sqrt{3}\alpha^2 a_r E\, k\, k_1}{6k_1 + (1+\nu)a_r^2}\right)\kappa. \tag{5.15}$$

Upon further inspection, the results of Eqs. 5.14 and 5.15 differ by a factor $a_r\alpha$. This term is negligible for small $a_r = b/h$ since α is already much smaller than unity. However when $a_r > \frac{1}{\alpha}$ the design would be based off of the normal bending moment instead of the binormal bending moment.

The tangent component of bending moment, M_t, develops shear stress in the spring. The shear stress developed in a spring with a rectangular cross section is determined using a similar procedure as in the axial load case. The maximum shear stress at $\theta = 90^o$ is

$$\tau_{max} = \frac{T}{8bh^2\, k_2(a_r)} = \frac{\beta\kappa}{8bh^2\, k_2(a_r)} = \left(\frac{2\sqrt{3}E\alpha k\, k_0 a_r}{6k_1 + (1+\nu)a_r^2}\right)\kappa \tag{5.16}$$

5.2.3 Stresses due to torsion

The stress due to torsional loading is approximated as bending of the coils in the binormal direction. The normal stress has the same form as in Eqs. 5.12 and 5.14 with the applied torque, T, in place of the bending moment, M.

Circular cross section

The normal stress from applied torsion in a spring with a circular cross section is

$$\sigma_{tt} = \frac{T\cos\alpha r}{I} = \frac{4T}{\pi r^3}. \tag{5.17}$$

Rectangular cross section

The normal stress from applied torsion in a spring with a rectangular cross section is

$$\sigma_{tt} = \frac{T\cos\alpha b}{I_b} = \frac{3T}{4hb^2} = \frac{\sqrt{3}Ta_r}{96k^3}. \tag{5.18}$$

5.3 Static design of helical springs for the SMA actuators

In order to develop a baseline design incorporating the various loads on the structure a static failure theory must be checked. The event of yielding would cause considerable damage to the actuator and a factor of safety must be maintained high in order to account for

approximations and uncertainty.

The stress components for the three types of loadings exhibited onto the helical spring were determined in Chapter 4. The combined effects of the various loadings are incorporated here into their von Mises components in order to generate design constraints [48]. The next two sections split those results between springs with circular and rectangular cross sections. In each section, design equations are developed.

The stress components for the spring are determined from the resultant loads on the structure from the external loads. The three components of bending moment will be considered to act on the cross section to produce normal and shear stresses which will contribute to the von Mises stress.

The von Mises stress can be calculated at the critical point in the cross section.

$$\sigma_1' = \sqrt{\sigma_t^2 + 3\tau_{nb}^2} \tag{5.19}$$

For the scope of this dissertation we have only addressed the static load design and future work on the fatigue analysis for springs should be completed in order to develop a full understanding of the design limitations. It is anticipated that fatigue will further limit the deformation and acceptable loads of the structure.

5.3.1 Circular cross section

For a spring with a circular cross section the stress state can be found by first considering the net moments acting throughout the structure. The resultant loads for a circular cross section can be simplified due to the rotational symmetry of the spring. The resultant moments which contribute to bending of the structure can be combined to yield one bending load. When this simplification is performed a method for finding the critical location of stress can be determined more readily.

$$M = \sqrt{M_n^2 + M_b^2} \tag{5.20}$$

Upon an expansion of the normal and binormal components in Eq. 5.20 we arrive at

$$M_c = M\sqrt{\cos^2\theta + (\sin\theta\sin\alpha + \gamma\cos\alpha)^2} \tag{5.21}$$

where the torsional magnitude coefficient, γ, has been introduced to account for the contribution of torsion. The effect of γ will change the critical location of stress and the overall stress magnitude.

Normal stress due to bending

The maximum normal stress due to bending is then found by applying the equation

$$\sigma_t = \frac{M_c r}{I} = \frac{4M_c}{\pi r^3}. \tag{5.22}$$

Since the equation for the critical bending moment, M_c, is in terms of variable θ we must determine the value of θ which maximizes the normal stress, but first we must incorporate

the effect of torsion to determine the critical location.

Shear stress due to torsion

The shear stress due to torsion of the cross section as determined in Eq. 5.13 is

$$\tau = \frac{(M_t)r}{J} = \frac{2M \sin\theta \cos\alpha}{\pi r^3}. \tag{5.23}$$

Design equations

The von Mises stress can now be determined as a function of θ. Applying Eq. 5.19 we arrive at

$$\sigma' = \sqrt{\sigma_t^2 + 3\tau^2} = \frac{2M}{\pi r^3}\sqrt{4\cos^2\theta + (\sin\theta \sin\alpha + \gamma\cos\alpha)^2 + 3(\sin\theta\cos\alpha)^2}. \tag{5.24}$$

The result of Eq. 5.24 requires that a maximum value must be determined at an unknown θ. In order to calculate this a derivative may be taken of the von Mises stress with respect to θ and these numerical solutions can be tested for whether they locate a maximum or minimum value of σ'. However a conservative estimate was found that greatly simplifies the calculation and does not require numerical methods.

The assumption that θ and α are small allows a small angle approximation for Eq. 5.24. The terms involving higher order terms of θ and α are considered negligible. To verify the approximation is conservative the function

$$\sigma' \approx \frac{2M}{\pi r^3}\sqrt{4 + \gamma^2} \tag{5.25}$$

The von Mises stress is then compared to the yield strength to ascertain the factor of safety. A value of of σ' less than the yield strength of the material is considered safe, but with a factor of safety greater than unity the design is more conservative.

$$\sigma' \leq S_y/n \tag{5.26}$$

In order to design the spring for our purposes we must determine a design equation with the previous developments and assumptions. Since the bending moment is applied to the spring when formed into a torus and when the torus is deflected as described in Chapter 2 we will utilize the bending stiffness and curvature to determine a design equation

$$\sigma' \approx \frac{2M}{\pi r^3}\sqrt{4+\gamma^2} = \frac{2\beta\kappa}{\pi r^3}\sqrt{4+\gamma^2} = \left(\frac{Er\alpha}{(2+\nu)}\right)(\sqrt{4+\gamma^2})\kappa \tag{5.27}$$

The form of σ' from Eq. 5.27 will now be substituted into Eq. 5.26. The assumed design variable is the radius of the spring, but the Young's modulus and Poisson's ratio are also likely design variables. Note that this equation is valid for an applied bending moment and torsion ($T = \gamma M$). Therefore γ acts as a ratio to the applied bending moment from curvature and can be substituted as needed. For a general nondimensional solution we can set $\tilde{\kappa} = \kappa r$, solve for $\tilde{\kappa}$ and determine the maximum value.

$$\sigma' = \left(\frac{E\alpha}{(2+\nu)}\right)(\sqrt{4+\gamma^2})\tilde{\kappa} < \frac{Sy}{n} \tag{5.28}$$

Rearranging Eq. 5.28 we can solve for the limiting value of $\tilde{\kappa}$.

$$\tilde{\kappa} < \left(\frac{Sy}{E\alpha n}\right)\left(\frac{(2+\nu)}{\sqrt{4+\gamma^2}}\right) \tag{5.29}$$

The ratio of yield strength over Young's modulus is an major component of the limiting value for $\tilde{\kappa}$. For steels this ratio varies slightly, but is typically around 0.25%. The helix angle, α, and factor of safety, n, are inversely proportional to $\tilde{\kappa}$ so an increase in either leads to a decrease in the nondimensional curvature allowed. Note that the mean radius, R, of the spring is not a factor in these equations, so for bending and torsion of a helical spring it evidently does not play an individual role in the strength design. However if the helix angle is in terms of helical pitch and mean radius we see that it does play a role (Eq. 5.30).

$$\tilde{\kappa} < \left(\frac{Sy}{En}\right)\left(\frac{2\pi R}{p}\right)\left(\frac{(2+\nu)}{\sqrt{4+\gamma^2}}\right) \tag{5.30}$$

It may be useful in the course of design to invert the curvature to design based on the radius of curvature. The radius of curvature, $\tilde{\rho}$, is

$$\tilde{\rho} = \frac{1}{\tilde{\kappa}} > \left(\frac{En}{Sy}\right)\left(\frac{p}{2\pi R}\right)\left(\frac{\sqrt{4+\gamma^2}}{(2+\nu)}\right). \tag{5.31}$$

This completes the stress based design of helical springs with circular cross sections. The values of $\tilde{\kappa}$ and γ can lead to a design for a given deformation and torque requirement.

5.3.2 Rectangular cross section

The rotational symmetry exhibited in a circular cross section does not exist in a rectangular cross section. The stress magnitude must be determined for various points on the exterior of the cross section since the normal stress due to bending and the shear stress due to torsion are maximal here. It will be shown that the situation is complicated by the application of γ and the aspect ratio, a_r.

Normal stress due to bending

The normal stress due to bending can be determined as a function of the normal and binormal moments applied to the cross section. The moment of inertia of a rectangle has two distinct values for the general case since the base, b, is not equal to the height, h, of the cross section.

$$\sigma_t = \frac{M_n z}{I_n} - \frac{M_b y}{I_b} \tag{5.32}$$

If the components for the normal and binormal moments and moments of inertia are substituted into Eq. 5.32 we arrive at

$$\begin{aligned} \sigma_t &= \frac{M(\cos\theta)z}{4/3bh^3} - \frac{M(\sin\theta\cos\alpha + \gamma\cos\alpha)y}{4/3bh^3} \\ &= \frac{3M}{4bh}\left(\frac{(\cos\theta)z}{h^2} - \frac{(\sin\theta\sin\alpha + \gamma\cos\alpha)y}{b^2}\right). \end{aligned} \tag{5.33}$$

Furthermore if we utilize the aspect ratio and radius of gyration as defined in Chapter 4 we can greatly reduce the complexity of the bending stress. In Eq. 5.34 the nondimensional terms $\tilde{z}$ and $\tilde{y}$ were introduced in order to develop a concept of magnitude. Note that both $\tilde{z}$ and $\tilde{y}$ have a range of -1 to 1.

$$\sigma_t = \frac{Ma_r}{32\sqrt{3}k^3}\left(a_r(\cos\theta)\tilde{z} - (\sin\theta\sin\alpha + \gamma\cos\alpha)\tilde{y}\right) \tag{5.34}$$

The normal stress is now in its final form and the shear stress due to torsion remains. This stress will involve calculations with infinite series as described earlier in this chapter.

Shear stress due to torsion

The shear stress due to torsion has two components which act in the plane of the cross section. For a rectangular cross section these components are maximal at the intersections of the exterior of the cross section and the axes of symmetry. These stresses are odd functions centered at the geometric center of the cross section.

The maximum components of shear stress are calculated at their corresponding locations. The two stresses are in terms of the infinite series representations, $k_2(a_r)$ and $k_3(a_r)$.

$$\tau_{xy}|_{\tilde{y}=0}^{\tilde{z}=1} = \frac{T}{8h^2bk_2(a_r)} = \frac{Ma_r^2(\sin\theta\cos\alpha + \gamma\cos\alpha)}{192\sqrt{3}k^3k_2(a_r)} \tag{5.35}$$

$$\tau_{zx}|_{\tilde{y}=1}^{\tilde{z}=0} = \frac{T}{8h^2bk_3(a_r)} = \frac{Ma_r^2(\sin\theta\cos\alpha + \gamma\cos\alpha)}{192\sqrt{3}k^3k_3(a_r)} \tag{5.36}$$

The shear stress correction, $k_3(a_r)$, is defined as

$$k_3(a_r) = \frac{8}{\pi^2}\left(\sum_{n=1}^{\infty}\frac{(-1)^{n-1}\tanh((2n-1)\pi a_r/2)}{(2n-1)^2}\right) \tag{5.37}$$

To appreciate the relative magnitude of stresses due to torsion of the rectangular section we can simply plot the ratio of shear corrections, k_2 to k_3 (Fig. 5.4). Note that the stress ratio ranges from unity to approximately 135%. This factor will play a role in the location of critical stress in the spring under bending and torsional loads.

The von Mises stress for a rectangular cross section is then determined at the two points of maximum shear stress. The normal stress due to bending has two components that are

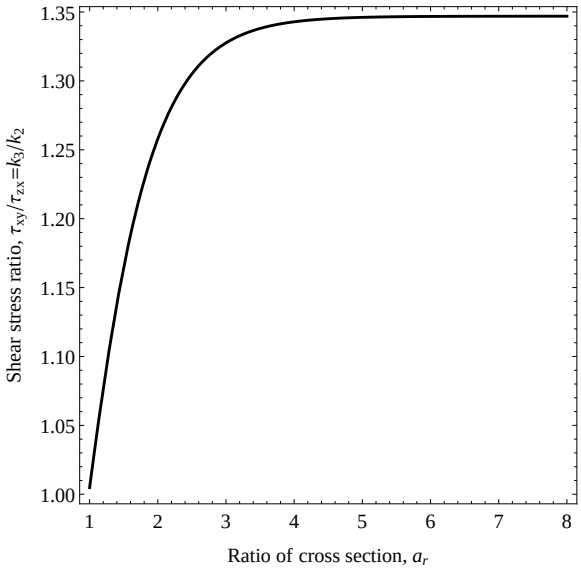

FIGURE 5.4: Relative magnitude of the shear stresses between the y faces and z faces

functions of $\tilde{y}$ and $\tilde{z}$ respectively. These components go to zero when either $\tilde{y}$ or $\tilde{z}$ go to zero. Therefore we determine the von Mises stress at these two points.

$$\sigma'|_{\tilde{y}=1}^{\tilde{z}=0} = \sqrt{\sigma_t^2 + 3\tau^2} = \frac{Ma_r^2}{32\sqrt{3}k^3}\sqrt{\frac{1}{a_r}(\sin\theta\sin\alpha + \gamma\cos\alpha)^2 + \frac{16}{3k_3(a_r)^2}(\sin\theta\cos\alpha)^2} \tag{5.38}$$

$$\sigma'|_{\tilde{y}=0}^{\tilde{z}=1} = \sqrt{\sigma_t^2 + 3\tau^2} = \frac{Ma_r^2}{32\sqrt{3}k^3}\sqrt{(\cos\theta)^2 + \frac{1}{12k_2(a_r)^2}(\sin\theta\cos\alpha)^2} \tag{5.39}$$

At this point we will again use a small angle approximation for α to reduce the complexity a bit.

$$\sigma'|_{\tilde{y}=1}^{\tilde{z}=0} = \frac{Ma_r^2}{32\sqrt{3}k^3}\sqrt{\frac{1}{a_r}(\alpha\gamma\sin\theta + \gamma^2) + \frac{16\sin^2\theta}{3k_3(a_r)^2}} \tag{5.40}$$

$$\sigma'|_{\tilde{y}=0}^{\tilde{z}=1} = \frac{Ma_r^2}{32\sqrt{3}k^3}\sqrt{(\cos\theta)^2 + \frac{\sin^2\theta}{12k_2(a_r)^2}} \tag{5.41}$$

Also it can be shown that the maximum values of von Mises stress occur when $\theta = \pi/2$ and $\sin\theta = 1$ and $\cos\theta = 0$.

$$\sigma'|_{\tilde{y}=1}^{\tilde{z}=0} = \frac{Ma_r^2}{32\sqrt{3}k^3}\sqrt{\frac{1}{a_r}(\alpha\gamma+\gamma^2)+\frac{16}{3k_3(a_r)^2}} \tag{5.42}$$

$$\sigma'|_{\tilde{y}=0}^{\tilde{z}=1} = \frac{Ma_r^2}{32\sqrt{3}k^3}\sqrt{\frac{1}{12k_2(a_r)^2}} \tag{5.43}$$

To determine which point will guide the design we first determine for what value of γ for which the two stresses are equal. Since the stress at both points has a common factor it can be ignored and the two radicals can be compared directly. The two sides can be squared to yield

$$\frac{2\alpha\gamma}{a_r}+\frac{\gamma^2}{a_r}+\frac{16}{3k_3^2} = \frac{1}{12k_2^2}. \tag{5.44}$$

Eq. 5.44 is in the form to solve for the two solutions for γ. The critical value of gamma can either be positive or negative which would correspond to positive or negative torques. The solutions for gamma are functions of the aspect ratio of the cross section and the helix angle (Eq. 5.45). The design regions for positive torques are displayed in Fig. 5.6.

$$\gamma_{crit} = -\alpha \pm \frac{\sqrt{a_r\left(k_3(a_r)^2 - 64k_2(a_r)^2\right)}}{2\sqrt{3}k_2(a_r)k_3(a_r)} \tag{5.45}$$

Design equations

For the case where $|\gamma| < |\gamma_{crit}|$ the design point is the top of the cross section ($\tilde{z} = 1, \tilde{y} = 0$). Similar to the procedure for the circular cross section we assure that the von Mises stress at

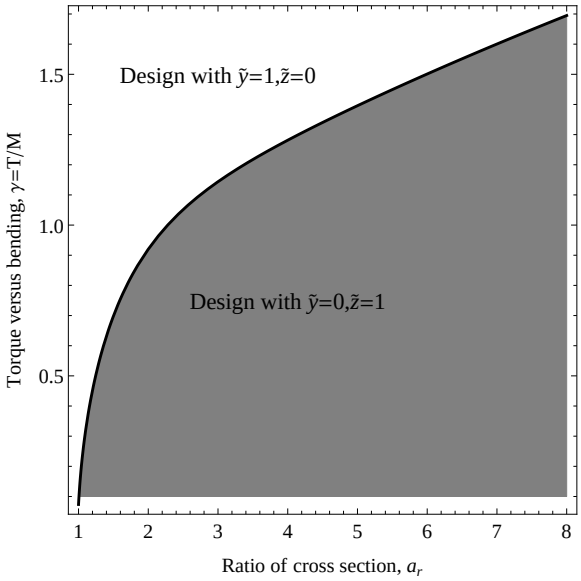

FIGURE 5.5: Critical torque to bending ratio

the critical location be less than the yield stress by some factor of safety.

$$\sigma'|_{\tilde{y}=0}^{\tilde{z}=1} = \frac{Sy}{n} = \frac{Ma_r^2}{192\sqrt{3}k_2(a_r)k^3} = \frac{\beta\kappa a_r^2}{192\sqrt{3}k_2(a_r)k^3} \tag{5.46}$$

We seek a form of Eq. 5.46 similar to the circular cross section design. Setting $\hat{\kappa} = k\kappa$ and solving for $\hat{\kappa}$ we obtain the following restriction on nondimensional curvature

$$\hat{\kappa} \leq \left(\frac{Sy}{E\alpha n}\right) \frac{6k_1(a_r) + a_r^2}{2\sqrt{3}a_r k_0(a_r)}. \tag{5.47}$$

For the case where $|\gamma| > |\gamma_{crit}|$ the point $(\tilde{z} = 0, \tilde{y} = 1)$ becomes the critical point and a similar procedure can be conducted were we determine a $\hat{\kappa}$ restriction. In order to visualize the effect of the critical point for γ see Fig. 5.6 or Fig. 5.7.

$$\hat{\kappa} \leq \left(\frac{Sy}{E\alpha n}\right) \frac{6k_1(a_r) + a_r^2}{12\sqrt{3}na_r k_1(a_r)\alpha\sqrt{\frac{2\alpha\gamma}{a_r} + \frac{\gamma^2}{a_r} + \frac{16}{3k_3(a_r)^2}}}. \tag{5.48}$$

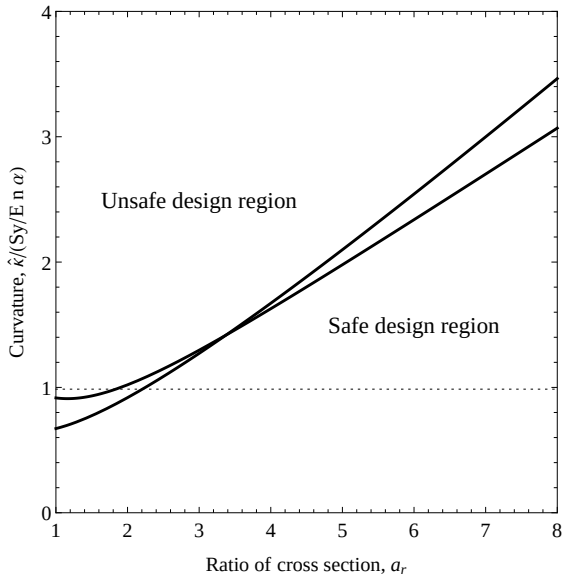

FIGURE 5.6: Curvature design for γ=1.5

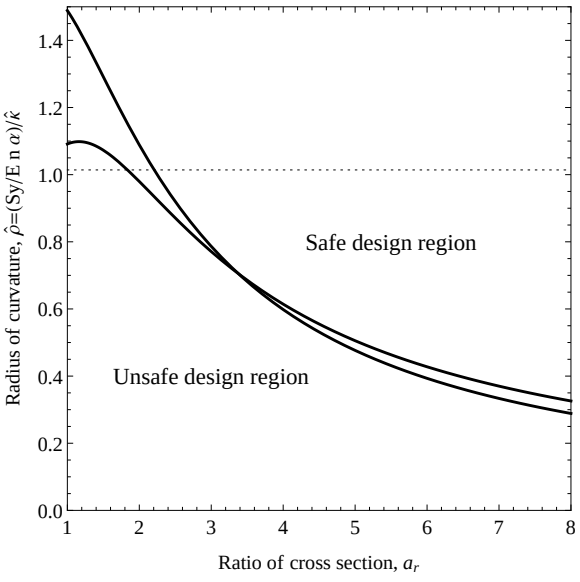

FIGURE 5.7: Radius of curvature design for γ=1.5

In the process of design it may be useful to develop a concept of radius of curvature for the springs in addition to the curvature itself. The relationship between the two is simply the radius of curvature is the inverse of the curvature and vice versa. In Fig. 5.6 and Fig. 5.7 the two solid lines represent the two functions which limit the radius of curvature for a rectangular spring. The dotted lines in those figures represent the limitation for a circular cross section.

This completes the stress design of helical springs with rectangular cross sections. The equations 5.47 and 5.48 can be used to determine allowable dimensions for a helical spring in bending and torsion. Note that the ratio of torsion to bending introduced a design switch at a critical value (Eq. 5.45).

Chapter 6

Conclusions and Additional Short Studies

6.1 Conclusions

Through the course of this dissertation the problem of actuation by means of a shape memory alloy embedded with a flexible matrix has been addressed. The complexities of the kinematics, equilibrium and application of rod theories were formulated and explained. The contributions of the work have resulted in a wider understanding of rod mechanics, helical springs and loose wire composites.

The benefits of using large deformation rod equations were demonstrated as the complex behavior of structures can be tracked in a deformed configuration. This has particular

usefulness in addressing the complexities of a shape memory alloy actuated structure.

We produced a model of a general spring that can be either an extension or compression spring with either circular or rectangular geometry. This expands the current research in the field in at least two different ways: firstly, we developed a contact condition and subsequent constitutive relations that couple bending and extension; secondly, the resulting model allows a continuum representation that can be applied to various problems involving springs under a wide range of conditions.

The helical spring was selected for a flexible backbone for the actuators due to functional design principles laid out in the last chapter. The static design of springs with circular and rectangular cross sections were developed in terms of the bending curvature, torsion and material properties. This contribution provides design equations for use in any bending spring application.

For both circular and rectangular springs a design range was determined based on static load magnitudes and bending and torsional deformation modes. The ratio of torsion to bending was demonstrated to play a large role in the case of the static design of springs with rectangular cross sections. Also the additional difficulties encountered when analyzing springs with rectangular cross sections were considered a worthwhile effort since the extra degrees of freedom allowed more selectivity in design and cover a wider range of applications. The added torsional rigidity and control over the relative stiffnesses make a rectangular spring an excellent candidate for the skeleton for the actuation strategy proposed herein.

Overall the contributions have provided a framework for subsequent development of actuators and the backbone design.

6.2 Other Studies

Several studies which have been conducted during my time here at Virginia Tech have not been presented in the bulk of this document, but have influenced the development of these works.

6.2.1 Heat transfer of SMA composite rod

Shape Memory Alloys produce constrained recovery forces due to the addition of heat and the change of phase. The actuators in this work are loaded cyclically, both in temperature and stress in order to evert the WSL robot. The heat transfer of this process is a limiting agent as the temperature in the wires must rise and fall at the rate required by the cyclic loading. The phase change in SMA materials is temperature dependent, so the cycle speed is reduced by the time required to heat and cool the wires.

In order to better understand the heat transfer in a SMA composite rod a Finite Element simulation was conducted to solve the problem of heat transfer in the axisymmetric case of the torus actuators. Both the steady state and transient solutions were computed and a preview of the results can be seen in Fig. 6.1.

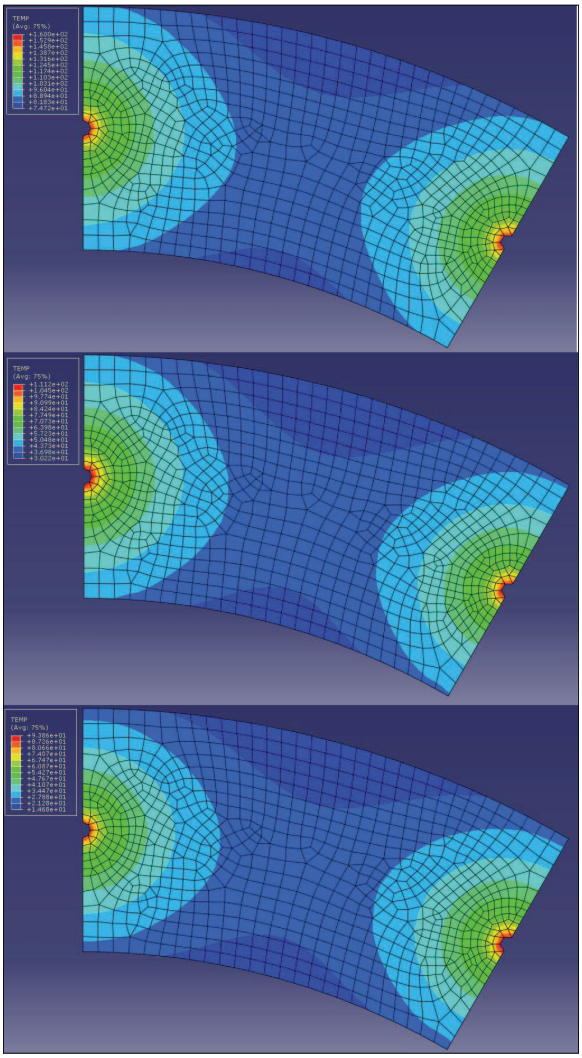

FIGURE 6.1: Effect of heat transfer coefficient on temperature distribution of actuator

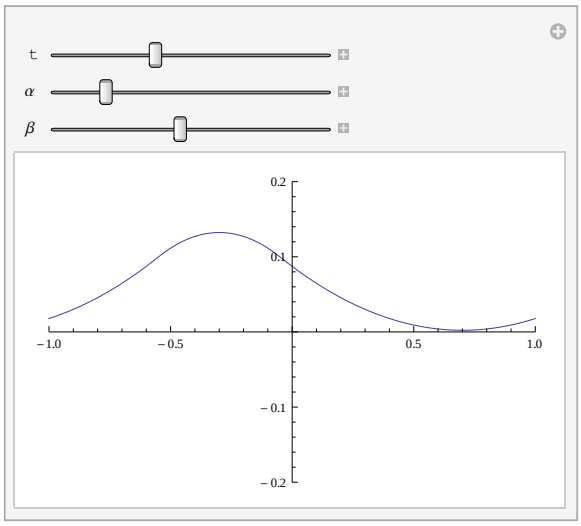

FIGURE 6.2: Fourier solution to steady state cyclic heating

A steady state solution of the moving heat source with periodic boundary conditions was also solved using Fourier analysis. The temperature of the tube was assumed to be constant through the thickness (small thickness of tube) and the heat loss on the exterior was due to convection. The non-dimensional solution for the assumed model can be seen in Fig. 6.2.

6.2.2 Bending of hollow tubes

Following the work of Wadee et al. [51], I conducted a nonlinear analysis of the deformed configuration of a hollow tube under pure bending. The shell equations were reduced to ODEs with an assumed modes solution as in Wadee et al. [51]. The solution of the nonlinear set of ODEs originating from this assumed modes form was solved using AUTO07p for various initial tube geometries. The hope of the study was to develop the critical bending moment as the tube deformed in its cross section. I replicated the non-homogeneity of the deformed

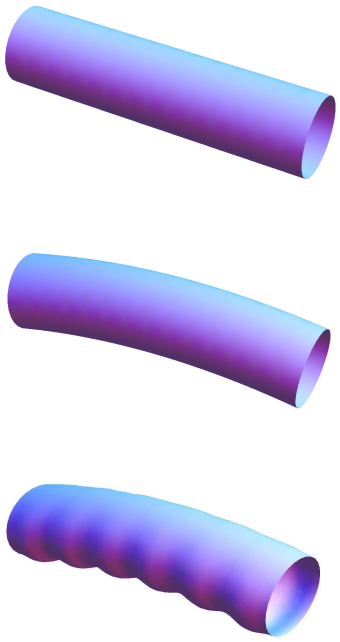

FIGURE 6.3: Nonhomogeneous bending of a tube

state that was proposed by Wadee in order to determine limit moments and curvatures for potential WSL actuator designs using tube structures.

The homogeneous problem of bending infinite tubes was also studied although the limiting curvatures were not within the limits of the actuator requirements.

The subsequent configurations of a rod found by the first study are depicted in Fig. 6.3.

6.2.3 Experimental Studies

The construction of several prototypes was conducted in order to generate proof of concepts for the actuation strategy of the SMA composite. Several PDMS-SMA composites were constructed.

The first of which was a solid PDMS cylinder with SMA wires embedded around the circumference of the cross section. This prototype demonstrated the ability to bend under load showing residual strains were generated in the manufacturing process. The bending stiffness of the solid PDMS cylinder was too high for significant actuation forces in the SMA wires.

The second prototype which was a hollow PDMS cylinder similarly configured as the first. The bending stiffness was of course reduced, however the torsional stiffness limited the ability to evert. Upon the bending of the actuator into the required arc, the wires tore through the PDMS layer. This demonstrated that the wire stress must be supported by a material that can withstand the distributed force from the wire.

A third prototype (pictured in Fig. 1.5) employed a compression spring to support the PDMS-SMA composite shell. This prototype demonstrated the ability to evert. The torsional rigidity of the shell was not sufficient to enable full eversion as the actuator wire pulled itself out of plane as was described in the previous chapter. This prototype eventually failed under similar conditions to the second prototype, so the use of PDMS was halted until further analyses could be completed.

6.3 Governing Equations of Rods in Deformed Coordinates

In Chapter 2, the governing equations of rods were developed. The main results of equilibrium kinematics, constitutive relations and equilibrium are displayed in a form convenient for simulations.

The dependent variables in the governing equations of rods are the displacements, $\vec{u}$, the curvatures, $\vec{\text{æ}}$, the force resultants, $\vec{Q}$, the moments, $\vec{M}$ and the Euler angles, θ_i. The set of equations are a system of nonlinear ODEs which can be solved using numerical methods.

The equations are now rewritten in a form conducive to solution via numerical methods.

6.3.1 Governing Equations for the General Deformations of Rods

$$\frac{dQ_1}{ds} = -Q_3æ_2 + Q_2æ_3 - P_1 \tag{6.1}$$

$$\frac{dQ_2}{ds} = -Q_1æ_3 + Q_3æ_1 - P_2 \tag{6.2}$$

$$\frac{dQ_3}{ds} = -Q_2æ_1 + Q_1æ_2 - P_3 \tag{6.3}$$

$$\frac{dM_1}{ds} = -M_3æ_2 + M_2æ_3 - T_1 \tag{6.4}$$

$$\frac{dM_2}{ds} = -M_1æ_3 + M_3æ_1 - T_2 + Q_3 \tag{6.5}$$

$$\frac{dM_3}{ds} = -M_2æ_1 + M_1æ_2 - T_3 - Q_2 \tag{6.6}$$

$$M_1 = A_{11}(æ_1 - æ_{01}) \tag{6.7}$$

$$M_2 = A_{22}(æ_2 - æ_{02}) \tag{6.8}$$

$$M_3 = A_{33}(æ_3 - æ_{03}) \tag{6.9}$$

$$\frac{d\theta_1}{ds} = -æ_{01} + æ_1\cos(\theta_2)\sec(\theta_3) + æ_3\sec(\theta_3)\sin(\theta_2) \tag{6.10}$$

$$-æ_{02}\cos(\theta_1)\tan(\theta_3) - æ_{03}\sin(\theta_1)\tan(\theta_3) \tag{6.11}$$

$$\frac{d\theta_2}{ds} = æ_2 - æ_{02}\cos(\theta_1)\sec(\theta_3) - æ_{03}\sec(\theta_3)\sin(\theta_1) \tag{6.12}$$

$$+æ_1\cos(\theta_2)\tan(\theta_3) + æ_3\sin(\theta_2)\tan(\theta_3) \tag{6.13}$$

$$\frac{d\theta_3}{ds} = -æ_{03}\cos(\theta_1) + æ_3\cos(\theta_2) + æ_{02}\sin(\theta_1) - æ_1\sin(\theta_2) \tag{6.14}$$

$$\frac{du_1}{ds} = 1 - l_{11} + u_2æ_3 - u_3æ_2 \tag{6.15}$$

$$\frac{du_2}{ds} = -l_{21} + u_3æ_1 - u_1æ_3 \tag{6.16}$$

$$\frac{du_3}{ds} = -l_{31} + u_1æ_2 - u_2æ_1 \tag{6.17}$$

6.3.2 Governing Equations for the Initially Straight Rods

$$\frac{dQ_1}{ds} = -Q_3\frac{M_2}{A_{22}} + Q_2\frac{M_3}{A_{33}} - P_1 \tag{6.18}$$

$$\frac{dQ_2}{ds} = -Q_1\frac{M_3}{A_{33}} + Q_3\frac{M_1}{A_{11}} - P_2 \tag{6.19}$$

$$\frac{dQ_3}{ds} = -Q_2\frac{M_1}{A_{11}} + Q_1\frac{M_2}{A_{22}} - P_3 \tag{6.20}$$

$$\frac{dM_1}{ds} = -T_1 \tag{6.21}$$

$$\frac{dM_2}{ds} = -T_2 + Q_3 \tag{6.22}$$

$$\frac{dM_3}{ds} = -T_3 - Q_2 \tag{6.23}$$

$$\frac{d\theta_1}{ds} = \frac{M_1}{A_{11}}\cos(\theta_2)\sec(\theta_3) + \frac{M_3}{A_{33}}\sec(\theta_3)\sin(\theta_2) \tag{6.24}$$

$$\frac{d\theta_2}{ds} = \frac{M_2}{A_{22}} + \frac{M_1}{A_{11}}\cos(\theta_2)\tan(\theta_3) + \frac{M_3}{A_{33}}\sin(\theta_2)\tan(\theta_3) \tag{6.25}$$

$$\frac{d\theta_3}{ds} = \frac{M_3}{A_{33}}\cos(\theta_2) - \frac{M_1}{A_{11}}\sin(\theta_2) \tag{6.26}$$

$$\frac{du_1}{ds} = 1 - l_{11} + u_2\frac{M_3}{A_{33}} - u_3\frac{M_2}{A_{22}} \tag{6.27}$$

$$\frac{du_2}{ds} = -l_{21} + u_3\frac{M_1}{A_{11}} - u_1\frac{M_3}{A_{33}} \tag{6.28}$$

$$\frac{du_3}{ds} = -l_{31} + u_1\frac{M_2}{A_{22}} - u_2\frac{M_1}{A_{11}} \tag{6.29}$$

6.3.3 Governing Equations for the Planar Deformations of Rods

The relations presented in the previous section may be greatly simplified if the problem is in plane deformation. In order for the rod to remain in a planar configuration, several

quantities must be identically zero. These quantities include M_1, M_2, Q_3, θ_1, θ_2 and u_3.

$$\frac{dQ_1}{ds} = Q_2 æ_3 - P_1 \tag{6.30}$$

$$\frac{dQ_2}{ds} = -Q_1 æ_3 - P_2 \tag{6.31}$$

$$\frac{dM_3}{ds} = -T_3 - Q_2 \tag{6.32}$$

$$\frac{d\theta_3}{ds} = æ_{03} + \frac{M_3}{A_{33}} \tag{6.33}$$

$$\frac{du_1}{ds} = 1 - \cos[\theta_3] + u_2 æ_3 \tag{6.34}$$

$$\frac{du_2}{ds} = -\sin[\theta_3] - u_1 æ_3 \tag{6.35}$$

$$M_3 = A_{33}(æ_3 - æ_{03}) \tag{6.36}$$

Bibliography

[1] Ingram, M., and Hong, D., 2005. "Whole Skin Locomotion Inspired by Amoeboid Motility Mechanisms". In 29th ASME Mechanisms and Robotics Conference, pp. 24–28.

[2] Hong, D., 2005. "A Biologically Inspired Whole Skin Locomotion Strategy for Mobile Robots". In US-Korea Conference on Science, Technology and Entrepreneurship.

[3] Granosik, G., Hansen, M. G., and Borenstein, J., 2005. "The OmniTread serpentine robot for industrial inspection and surveillance". *Industrial Robot: An International Journal,* ***32***(2), pp. 139–148.

[4] Goldman, R. E. R., Fine, H. F. H., Simaan, N., Wei, W., and Chang, S., 2009. "Performance Evaluation for Multi-arm Manipulation of Hollow Suspended Organs". *IEEE Transactions on Robotics,* ***25***(1), Feb., pp. 147–157.

[5] Mahvash, M., and Dupont, P. E., 2010. "Stiffness Control of a Continuum Manipulator in Contact with a Soft Environment.". *Proceedings of the ... IEEE/RSJ International*

Conference on Intelligent Robots and Systems. IEEE/RSJ International Conference on Intelligent Robots and Systems, ***2010***, Dec., pp. 863–870.

[6] Kassim, I., Phee, L., Ng, W. S., Gong, F., Dario, P., and Mosse, C. a., 2006. "Locomotion techniques for robotic colonoscopy.". *IEEE engineering in medicine and biology magazine : the quarterly magazine of the Engineering in Medicine & Biology Society,* ***25***(3), pp. 49–56.

[7] Toennies, J. L., Tortora, G., Simi, M., Valdastri, P., and Iii, R. J. W., 2009. "Swallowable medical devices for diagnosis and surgery : the state of the art". *Mechanical Engineering Science,* ***224***, pp. 1397–1414.

[8] Breedveld, P., 2006. "Development of a Rolling Stent Endoscope". *The First IEEE/RAS-EMBS International Conference on Biomedical Robotics and Biomechatronics*, pp. 921–926.

[9] Wakasa, Y., Oka, M., Tanaka, K., Fujii, M., Yamauchi, S., and Minami, K., 2006. "Development of a Needle-Insertion Robot for MRI-Guided Stereotactic Surgery". *Journal of Robotics and Mechatronics*, pp. 643–644.

[10] Utter, B., Barnes, B., Luntz, J., and Brei, D., 2010. "Design of an SMA Actuated Mechanotransductive Implant for Correcting Short Bowel Syndrome". In 2010 ASME Conference on Smart Materials, Adaptive Structures and Intelligent Systems, pp. 1–18.

[11] Mckenna, J. C., Anhalt, D. J., Bronson, F. M., Brown, H. B., Schwerin, M., and Choset, H., 2008. "Toroidal Skin Drive for Snake Robot Locomotion". *2008 IEEE International Conference on Robotics and Automation*, pp. 1150–1155.

[12] Webster, R. J., 2007. "Design and Mechanics of Continuum Robots for Surgery". PhD thesis, The Johns Hopkins University.

[13] Wei, W., Goldman, R., Simaan, N., Fine, H., and Chang, S., 2007. "Design and Theoretical Evaluation of Micro-Surgical Manipulators for Orbital Manipulation and Intraocular Dexterity". *Proceedings 2007 IEEE International Conference on Robotics and Automation*(April), Apr., pp. 3389–3395.

[14] Ota, T., Degani, A., Schwartzman, D., Zubiate, B., McGarvey, J., Choset, H., and Zenati, M. a., 2009. "A highly articulated robotic surgical system for minimally invasive surgery.". *The Annals of thoracic surgery,* ***87***(4), Apr., pp. 1253–6.

[15] Rucker, D. C., Jones, B. a., and Webster, R. J., 2010. "A Geometrically Exact Model for Externally Loaded Concentric-Tube Continuum Robots.". *IEEE transactions on robotics : a publication of the IEEE Robotics and Automation Society,* ***26***(5), Jan., pp. 769–780.

[16] Xu, K., and Simaan, N., 2010. "Intrinsic Wrench Estimation and Its Performance Index for Multisegment Continuum Robots". *IEEE Transactions on Robotics,* ***26***(3), pp. 555–561.

[17] Lotti, F., Tiezzi, P., Vassura, G., Biagiotti, L., Palli, G., and Melchiorri, C. "Development of UB Hand 3: Early Results". *Proceedings of the 2005 IEEE International Conference on Robotics and Automation*, pp. 4488–4493.

[18] Lotti, F., and Vassura, G., 2002. "A novel approach to mechanical design of articulated fingers for robotic hands". *IEEE/RSJ International Conference on Intelligent Robots and System*, pp. 1687–1692.

[19] Reggiani, B., 2007. "Simulation Models in Biomechanics and Experimental Mechanics". PhD thesis, University of Bologna.

[20] Li, C., and Rahn, C. D., 2002. "Design of Continuous Backbone, Cable-Driven Robots". *Journal of Mechanical Design,* ***124***(2), p. 265.

[21] Camarillo, D. B., Milne, C. F., Carlson, C. R., Zinn, M. R., and Salisbury, J. K., 2008. "Mechanics Modeling of Tendon-Driven Continuum Manipulators". *IEEE Transactions on Robotics,* ***24***(6), Dec., pp. 1262–1273.

[22] Ilievski, F., Mazzeo, A. D., Shepherd, R. F., Chen, X., and Whitesides, G. M., 2011. "Soft robotics for chemists.". *Angewandte Chemie (International ed. in English),* ***50***(8), Feb., pp. 1890–5.

[23] Dupont, P. E., Lock, J., Itkowitz, B., and Butler, E., 2010. "Design and Control of Concentric-Tube Robots.". *IEEE transactions on robotics : a publication of the IEEE Robotics and Automation Society,* ***26***(2), Apr., pp. 209–225.

[24] Kumar, P., and Lagoudas, D., 2008. "Introduction to Shape Memory Alloys". In *Shape Memory Alloys Modeling and Engineering Applications*, D. Lagoudas, ed. Springer, pp. 1–51.

[25] Turner, T. L., 2001. "Fabrication and characterization of SMA hybrid composites". *Proceedings of SPIE,* ***4333***(4333), pp. 343–354.

[26] Hartl, D. J., Lagoudas, D. C., Calkins, F. T., and Mabe, J. H., 2010. "Use of a Ni60Ti shape memory alloy for active jet engine chevron application: I. Thermomechanical characterization". *Smart Materials and Structures,* ***19***(1), Jan., p. 015020.

[27] Sreekumar, M., Nagarajan, T., Singaperumal, M., Zoppi, M., and Molfino, R., 2007. "Critical review of current trends in shape memory alloy actuators for intelligent robots". *Industrial Robot: An International Journal,* ***34***(4), pp. 285–294.

[28] Dupont, P., Armstrong, B., and Hayward, V., 2004. "Elasto-plastic friction model: contact compliance and stiction". *Proceedings of the 2000 American Control Conference. ACC (IEEE Cat. No.00CH36334),* ***2***(2), pp. 1072–1077.

[29] Antman, S. S., 2005. *Nonlinear Problems of Elasticity*, 2nd ed., Vol. 107. Springer-Verlag, New York.

[30] Grigolyuk, E., and Shalashilin, V., 1991. *Problems of Nonlinear Deformation: The Continuation Method Applied to Nonlinear Problems in Solid Mechanics*. Kluwer Academic Publishers, Norwell, MA.

[31] Love, A. E. H., 1944. *A Treatise on the Mathematical Theory of Elasticity*, 4th ed. Dover.

[32] Green, A., and Zerna, W., 1992. *Theoretical Elasticity*. Dover Publications, New York.

[33] Svetlitsky, V., 2000. *Statics of Rods*. Springer-Verlag, New York.

[34] Svetlitsky, V., 2005. *Dynamics of Rods*. Springer, New York.

[35] Tadjbakhsh, I., and Lagoudas, D., 1994. "Variational theory of motion of curved, twisted and extensible elastic rods". *International Journal of Engineering Science,* ***32***(4), Apr., pp. 569–577.

[36] McConnell, A., 1957. *Applications of Tensor Analysis*. Dover, Toronto.

[37] Kreyszig, E., 1991. *Differential geometry*. Dover, New York.

[38] Stoker, J., 1969. *Differential Geometry*. Wiley-Interscience, New York.

[39] Truesdell, C., and Toupin, R., 1960. "The Classical Field Theories". In *Encyclopedia of Physics III/1*, S. Flugge, ed. Springer-Verlag, New York, pp. 227–850.

[40] Tadjbakhsh, Iradj and Lagoudas, D., 1993. "Deformations of active flexible rods with embedded line actuators". *Smart Materials and Structures,* ***71***(2), pp. 71–81.

[41] Turner, T. L., 2000. "A New Thermoelastic Model for Analysis of Shape Memory Alloy Hybrid Composites". *Journal of Intelligent Material Systems and Structures,* ***11***(5), May, pp. 382–394.

[42] Veeramani, A. S., Buckner, G. D., Owen, S. B., Cook, R. C., and Bolotin, G., 2008. "Modeling the dynamic behavior of a shape memory alloy actuated catheter". *Smart Materials and Structures,* ***17***, pp. 1–14.

[43] Hyer, M., 2009. *Stress Analysis of Fiber-reinforced Composite Materials.* DEStech Publications.

[44] Jonnalagadda, K., Kline, G., and Sottos, N., 1997. "Local Displacements and Load Transfer in Shape Memory Alloy Composites". *Experimental Mechanics,* ***37***(1), pp. 78–86.

[45] Timoshenko, S. P., 1953. *History of Strength of Materials.* McGraw Hill, New York.

[46] Wahl, A., 1963. *Mechanical Springs*, 2nd ed. McGraw Hill.

[47] Timoshenko, S., 1976. *Strength of Materials*, 3rd ed. Krieger Publishing Co., Huntington, NY.

[48] Nisbett, R. G. B., and Keith, J., 2011. *Shigley's mechanical engineering design.* McGraw Hill, New York, NY.

[49] Boresi, A., and Schmidt, R., 2003. *Advanced Mechanics of Materials.* John Wiley & Sons, Hoboken, NJ.

[50] Stakenborg, M., 1988. "On the sealing mechanism of radial lip seals". *Tribology,* ***21***(6), pp. 335–340.

[51] Wadee, M. K., Wadee, M. A., and Bassom, A. P., 2007. "Effects of orthotropy and variation of Poisson's ratio on the behaviour of tubes in pure flexure". *Journal of the Mechanics and Physics of Solids,* ***55***(5), May, pp. 1086–1102.